The Astrophysical Journal, 960:74 (16pp), 2024 January 1 https://doi.org/10.3847/1538-4357/ad03e8

High-energy Neutrinos from Gamma-Ray-faint Accretion-powered Hypernebulae

Navin Sridhar[1,2], Brian D. Metzger[2,3,4], and Ke Fang[5]
[1] Department of Astronomy, Columbia University, New York, NY 10027, USA; navin.sridhar@columbia.edu
[2] Theoretical High Energy Astrophysics (THEA) Group, Columbia University, New York, NY 10027, USA
[3] Department of Physics, Columbia University, New York, NY 10027, USA
[4] Center for Computational Astrophysics, Flatiron Institute, New York, NY 10010, USA
[5] Department of Physics, Wisconsin IceCube Particle Astrophysics Center, University of Wisconsin, Madison, WI 53706, USA
Received 2022 December 21; revised 2023 September 19; accepted 2023 October 15; published 2023 December 27

Abstract

Hypernebulae are inflated by accretion-powered winds accompanying hyper-Eddington mass transfer from an evolved post-main-sequence star onto a black hole or neutron star companion. The ions accelerated at the termination shock—where the collimated fast disk winds and/or jet collide with the slower, wide-angled wind-fed shell—can generate high-energy neutrinos via hadronic proton–proton reactions, and photohadronic ($p\gamma$) interactions with the disk thermal and Comptonized nonthermal background photons. It has been suggested that some fast radio bursts (FRBs) may be powered by such short-lived jetted hyper-accreting engines. Although neutrino emission associated with the millisecond duration bursts themselves is challenging to detect, the persistent radio counterparts of some FRB sources—if associated with hypernebulae—could contribute to the high-energy neutrino diffuse background flux. If the hypernebula birth rate follows that of stellar-merger transients and common envelope events, we find that their volume-integrated neutrino emission—depending on the population-averaged mass-transfer rates—could explain up to ∼25% of the high-energy diffuse neutrino flux observed by the IceCube Observatory and the Baikal Gigaton Volume Detector Telescope. The time-averaged neutrino spectrum from hypernebula—depending on the population parameters—can also reproduce the observed diffuse neutrino spectrum. The neutrino emission could in some cases furthermore extend to >100 PeV, detectable by future ultra-high-energy neutrino observatories. The large optical depth through the nebula to Breit–Wheeler ($\gamma\gamma$) interaction attenuates the escape of GeV–PeV gamma rays coproduced with the neutrinos, rendering these gamma-ray-faint neutrino sources, consistent with the Fermi observations of the isotropic gamma-ray background.

Unified Astronomy Thesaurus concepts: Neutrino astronomy (1100); High energy astrophysics (739); Shocks (2086); X-ray binary stars (1811); Ultraluminous x-ray sources (2164); Nebulae (1095); Compact nebulae (287); Jets (870); Particle astrophysics (96); Plasma astrophysics (1261); High mass x-ray binary stars (733); Binary stars (154)

1. Introduction

The IceCube Observatory, and recently, the Baikal Gigaton Volume Detector Telescope measured the flux and spectrum of the diffuse high-energy (TeV-100 PeV; HE, hereafter) neutrino background, finding an all-flavor all-sky-averaged flux of $\sim 5 \times 10^{-8}\,\mathrm{GeV\,s^{-1}\,cm^{-2}\,sr^{-1}}$ at 100 TeV (IceCube Collaboration et al. 2001, 2018a; Abbasi et al. 2021a, 2022; Baikal Collaboration et al. 2023). The sensitivity limits of the current neutrino facilities have not allowed for the detection of the long sought-after ultra-high-energy (⩾100 PeV; UHE, hereafter) neutrinos. The detected HE neutrinos may plausibly be produced in baryonic shocks: one of the consequences of magnetized shocks of electron-ion plasmas is the nonthermal acceleration of ions to relativistic energies via diffusive shock acceleration (DSA; Blandford & Ostriker 1978; and also via turbulence, for example, Comisso & Sironi 2022). Such relativistic ions can generate neutrinos via hadronuclear proton–proton (pp), and photohadronic ($p\gamma$) interactions (e.g., Waxman & Bahcall 1997; Mészáros & Waxman 2001; Dermer & Atoyan 2003; Guetta & Granot 2003). The contribution from the Galactic plane to the all-sky neutrino flux is found to be ≲5%–10% at around 100 TeV, suggesting that most of the observed apparently isotropic diffuse neutrino flux is extragalactic (Aartsen et al. 2017; Albert et al. 2018; Fang & Murase 2021). There has been evidence for at least one gamma-ray blazar, TXS 0506+056, contributing to the neutrino signal (IceCube Collaboration et al. 2018b, 2018c). Recently, the 10 yr point-source searches with IceCube have indicated that the type-II Seyfert starburst galaxy NGC 1068 is the most significant (at 4.2σ) steady source of neutrinos (Aartsen et al. 2020; IceCube Collaboration et al. 2022). However, in their respective energy ranges, NGC 1068 and TXS 0506 + 056 contribute no more than ∼1% above 10 TeV to the overall HE diffuse background neutrino flux.

Therefore, the sources for the majority of the extragalactic background neutrinos still remain a mystery. Various astrophysical objects have been studied as the sources of the HE neutrinos, such as gamma-ray bursts (GRBs; Paczynski & Xu 1994; Waxman & Bahcall 1997; Mészáros & Waxman 2001; Dermer & Atoyan 2003; Fasano et al. 2021; Kimura 2022), active galactic nuclei (AGN; Eichler 1979; Stecker et al. 1991; Jacobsen et al. 2015; Murase 2017; Kun et al. 2022), different kinds of supernovae (SNe; Razzaque et al. 2004; Murase et al. 2011; Murase 2018; Grichener & Soker 2021; Chang et al. 2022; Sarmah et al. 2022; Abbasi et al. 2023b), bubbles associated with ultraluminous X-ray (ULX) sources (Inoue et al. 2017), starburst galaxies (Romero & Torres 2003; Loeb & Waxman 2006; Thompson et al. 2006),

tidal disruption events (Senno et al. 2015; Wang & Liu 2016; Dai & Fang 2017; Lunardini & Winter 2017; Senno et al. 2017), nonrelativistic shock-powered transients (such as, e.g., luminous red novae, fast blue optical transients, hereafter FBOTs; Fang et al. 2020), fast radio bursts (FRBs; Metzger et al. 2020), proto-magnetars (Bhattacharya et al. 2023), supermassive black hole mergers (Jaroschewski et al. 2023), collapsars (Guo et al. 2023), among other sources. However, the stacking analysis with IceCube and ANTARES has shown that none of the above sources are likely to contribute a major fraction of the all-sky neutrino flux (Aartsen et al. 2016; Albert et al. 2021; Liodakis et al. 2022).

The HE diffuse background neutrino flux is comparable to that of UHE cosmic rays and gamma rays, hinting at a possible common origin. This is expected because a comparable flux of gamma rays will also be produced with neutrinos following both the proton–proton (pp) and proton–photon ($p\gamma$) interactions. But, the diffuse isotropic gamma-ray background (IGRB; subtracting the contributions from resolved sources, foreground emission, and unresolved blazars) observed by Fermi Large Area Telescope (LAT) between 100 MeV and 1 TeV (Ackermann et al. 2015) has disfavored gamma-ray bright sources being dominant sources of HE neutrinos, i.e., at lower energies, there is more neutrino flux than the corresponding gamma-ray flux if they were produced by the same sources through the pp or $p\gamma$ channels (Abbasi et al. 2021b). This fact that the all-sky neutrino flux at 10 TeV is larger than the expected gamma-ray flux (from an accelerated proton with a power-law index of -2) suggests that the dominant source of the HE diffuse background neutrino flux must be opaque to GeV–TeV gamma rays (Murase et al. 2016; Capanema et al. 2020, 2021; Fang et al. 2022).

Such requirements could naturally be met by the new class of astrophysical objects called "hypernebulae" (Sridhar & Metzger 2022). A hypernebula is an energetic, compact *bubble* ($\lesssim$1 pc; much smaller and powerful than the nebulae surrounding typical ULX sources) of plasma inflated into the circumbinary medium through shocks by powerful accretion disk winds and jets during the dynamically unstable (or even thermal-timescale) transfer of matter onto a compact object (black hole or neutron star) at rates that exceed the Eddington rate by many orders of magnitude. Such brief phases of rapid mass transfer are expected to occur following the Roche-lobe overflow from a donor star, prior to a common-envelope merger event and the "intermediate luminosity optical transients" accompanying it (such as luminous red novae; Soker 2022; and FBOTS, Prentice et al. 2018; Perley et al. 2019; Ho et al. 2020). The compact object, upon entering the common envelope, can continue accreting matter from the stellar envelope and launch jets, where accelerated protons can generate neutrinos via photohadronic interactions (Grichener & Soker 2021). Recently, Sridhar et al. (2021a) showed that the flaring collimated jets launched by the compact object at the heart of such accreting engines could power the (periodically) repeating FRBs. The radio-bright hypernebulae surrounding them could be the source of the persistent radio emission seen spatially coincident with FRBs (Chatterjee et al. 2017; Niu et al. 2022), which also imparts the rotation measure onto the pulses propagating through them (Sridhar & Metzger 2022). In fact, hypernebulae could already be present in blind wide-field radio surveys such as Faint Images of the Radio Sky at Twenty cm (FIRST; Becker et al. 1995) and VLASS (Lacy et al. 2020) as off-nuclear radio sources, and could be spatially resolved by the next generation Very Large Array (Selina et al. 2018).

In this paper, we investigate the properties of the ions accelerated at the different shock fronts present in hypernebulae, and their interactions with other ions (pp) and the *background* disk thermal and Comptonized nonthermal UV and/or X-ray photons ($p\gamma$). Such interactions could produce pions, which subsequently decay into neutrinos and gamma rays. We show that the HE neutrinos generated by hypernebulae could explain—depending on the mass-transfer rates achieved in typical sources—a significant fraction ($\gtrsim$25%) of the observed extragalactic HE diffuse neutrino background. The dense environment present in hypernebulae further attenuates the >TeV gamma rays produced by pion decay, thus rendering them gamma-ray faint. In Section 2, we discuss the nature of the outflows from the accreting engine: properties of the shocks and their associated timescales (Section 2.1), and the sources of background radiation (Section 2.2). The model for neutrino production is presented in Section 3, with discussions on pion production channels (Section 3.1), pion production efficiency (Section 3.2), ion heating and acceleration (Section 3.3), and neutrino production from pion decay (Section 3.4). We present some observational implications of our model in Section 4 before concluding in Section 5.

2. Properties of the Engine

As discussed in Sridhar & Metzger (2022), at least three different types of disk and/or jet outflow interactions can occur in hypernebulae: (1) The slow, wide-angled winds from the black hole and/or neutron star accretion disk interacting with the circumstellar medium (CSM) via a subrelativistic forward shock (FS); the location of this shell—that sweeps up both the wind material and the CSM—controls the overall radius of the system and, hence, the gas and X-ray photon number density within the hypernebula. (2) The trailing slow winds colliding with the accumulated shell ahead of them, forming what we call the *wind termination shock* (WTS). (3) Faster winds and/or jet from the innermost regions of the accretion flow, directed along the instantaneous (and likely precessing) angular momentum axis of the inner disk and/or jet, inflate bipolar lobes upon their interaction with the swept-up shell, mediated by what we call the *jet termination shock* (JTS). We refer the reader to Figure 1 of Sridhar & Metzger (2022) for a schematic diagram of the hypernebula and these various interaction fronts.

Our assumed fiducial model parameters, corresponding to a high-mass X-ray binary, are as follows [with the explored parameter range given in square brackets]. The central compact object is fiducially assumed to be a black hole of mass $m_\bullet = M_\bullet/M_\odot = 10$, experiencing mass-transfer at a rate of $\dot{m} = \dot{M}/\dot{M}_{\rm Edd} = 10^5$ [10^3, 10^7][6] from an evolved companion star of mass, $m_\star = M_\star/M_\odot = 30$. The accretion disk drives a wide-angled "slow" wind of average velocity $v_{\rm w}/c = 0.03$ [0.01, 0.1], and kinetic luminosity $L_{\rm w} = \dot{M}_{\rm w} v_{\rm w}^2/2$, as well as a "fast" wind and/or jet from the innermost regions of the disk with a speed $v_{\rm j}/c = 0.3$ [0.1, 0.5] (Kobayashi et al. 2018; Urquhart et al. 2018; Pinto & Kosec 2023). The mass-loss rate in the wide-angled disk winds is assumed to equal the mass-transfer rate $\dot{M}_{\rm w} \approx \dot{m}$ (Hashizume et al. 2015), while that in the jet is taken to be $\dot{M}_{\rm j} = \eta \dot{M}_{\rm w} (v_{\rm w}/v_{\rm j})^2$, with $\eta = 0.5$ [0.1, 1] expected from radiatively inefficient super-Eddington accretion disk models, due to the roughly equal gravitational energy

[6] $\dot{M}_{\rm Edd} = L_{\rm Edd}/(0.1c^2)$ is the Eddington accretion rate, and $L_{\rm Edd} \simeq 1.5 \times 10^{39} (m_\bullet/10) {\rm erg\ s^{-1}}$.

released per radial decade in the accretion flow (Blandford & Begelman 1999). We define the jet magnetization parameter $\sigma_j = 0.1$ [0.01, 1] as the ratio of its Poynting to kinetic energy flux. The density of the external CSM with which the wind-shell interacts is $\rho_{csm} = \mu n m_p$, where $n = 10\,[1,\ 100]\,\mathrm{cm}^{-3}$, typical of the massive-star environments (Abolmasov et al. 2008; Pakull et al. 2010; Toalá & Arthur 2011), and $\mu = 1.38$ is the mean atomic weight.

2.1. Ejecta

Mass-transfer from a donor star that has evolved off the main sequence can under some circumstances become unstable, ultimately culminating in a merger or common-envelope event (e.g., Roepke & De Marco 2023). However, prior to this final phase, the compact object can experience a high mass-transfer rate $\dot{M}$, lasting for a duration up to

$$t_{active} \sim \frac{M_\star}{\dot{M}} \approx 10^3\ \mathrm{yr}\left(\frac{m_\star}{30}\right)\dot{m}_5^{-1}, \tag{1}$$

where $\dot{m}_5 \equiv \dot{M}/(10^5 \dot{M}_{Edd})$. This *active time*, which precedes the final dynamical phase, corresponds to the lifetime of the jet inflating the hypernebula. The ejecta freely expands until the mass released in the accretion disk winds becomes comparable to that accumulated from the CSM, on the timescale (Sridhar & Metzger 2022)

$$t_{free} \approx 80\ \mathrm{yr}\left(\frac{L_{w,42}}{n_1}\right)^{1/2} v_{w,9}^{-5/2}. \tag{2}$$

Unless otherwise specified, we shall normalize analytical estimates to $t = t_{free}$ throughout the rest of the paper, using the shorthand notation $Y_x \equiv Y/10^x$ in cgs units for quantities other than $\dot{m}$.

At times $t \gtrsim t_{free}$, the nebula enters a self-similar deceleration phase (Weaver et al. 1977). The temporal evolution of the radius of the shell—bridging the two phases across t_{free}—can be approximated as

$$R(t) \simeq \begin{cases} v_w t \approx 0.75\ \mathrm{pc}\ v_{w,9}\left(\dfrac{t}{80\ \mathrm{yr}}\right) & (t < t_{free}) \\ \alpha\left(\dfrac{L_w t^3}{\rho_{csm}}\right)^{1/5} \approx 0.75\ \mathrm{pc}\left(\dfrac{L_{w,42}}{n_1}\right)^{1/5}\left(\dfrac{t}{80\ \mathrm{yr}}\right)^{3/5} & (t > t_{free}), \end{cases} \tag{3}$$

where $\alpha \approx 0.88$ while the FS is adiabatic, and $\alpha \approx 0.76$ after it becomes radiative (Weaver et al. 1977).[7] The shell expands at roughly the FS velocity

$$v_{fs} = \frac{dR}{dt} \approx 10^9\ \mathrm{cm\ s^{-1}} \times \begin{cases} v_{w,9} & (t < t_{free}) \\ \left(\frac{L_{w,42}}{n_1}\right)^{1/5}\left(\frac{t}{80\ \mathrm{yr}}\right)^{-2/5} & (t > t_{free}), \end{cases} \tag{4}$$

with the corresponding expansion timescale,

$$t_{exp} \simeq \frac{R}{v_{fs}} \simeq 80\ \mathrm{yr}\left(\frac{t}{80\ \mathrm{yr}}\right). \tag{5}$$

[7] As we show below, for the cases of interest $\dot{m} > 10^3$, the FS does not become radiative on the active duration.

As the shell expands, it accumulates a mass

$$M_{sh} \simeq \begin{cases} \dot{M}_w t \approx 2\ M_\odot \dot{m}_5\left(\dfrac{t}{80\ \mathrm{yr}}\right) & (t < t_{free}) \\ (4\pi/3)\rho_{csm} R^3 \approx 2\ M_\odot L_{w,42}^{3/5} n_1^{2/5}\left(\dfrac{t}{80\ \mathrm{yr}}\right)^{9/5} & (t > t_{free}) \end{cases}. \tag{6}$$

At later times ($t > t_{free}$), the swept-up mass from the CSM grows rapidly as $t^{9/5}$, dominating the mass injected by the disk wind. The mean baryon density of the shell is given by

$$n_p \simeq \frac{3M_{sh}}{4\pi R^2 m_p \mu dR} \approx \begin{cases} 30\ \mathrm{cm^{-3}}\ \dot{m}_5 v_w^{-3}\left(\frac{t}{80\ \mathrm{yr}}\right)^{-2} & (t < t_{free}) \\ 10\ \mathrm{cm^{-3}}\ n_1 & (t > t_{free}), \end{cases} \tag{7}$$

where we have assumed shell radial thickness $dR \sim R$, as expected for an adiabatic shock in which the post-shock gas does not cool rapidly (see below). This density is substantially lower, for example, than in a magnetar wind nebula (Fang & Metzger 2017) during its active neutrino production phase ($\lesssim$1 yr after magnetar birth), with implications for the interaction channels through which neutrinos are produced (see Section 3.2 for further discussion).

The kinetic luminosity of the different shock fronts are approximately given by

$$L_s \approx \frac{9\pi}{8}R^2 \times \begin{cases} \rho_{fs} v_{fs}^3 & (\mathrm{FS}) \\ \rho_{wts}(v_w - v_{fs})^3 & (\mathrm{WTS}) \\ \rho_{jts}(v_j - v_{fs})^3 & (\mathrm{JTS}), \end{cases} \tag{8}$$

where the upstream gas densities entering the above expressions are $\rho_{fs} = \rho_{csm}$, $\rho_{wts} = \dot{M}_w/(4\pi v_w R^2)$, and $\rho_{jts} = \dot{M}_j/(4\pi v_j R^2)$, respectively. At $t > t_{free}$, the particles behind each shock are heated to mean energies,

$$\bar{E} \approx \frac{3}{16}\mu m_p \times \begin{cases} v_{fs}^2 \approx 220\ \mathrm{keV}\left(\dfrac{L_{w,42}}{n_1}\right)^{2/5}\left(\dfrac{t}{80\ \mathrm{yr}}\right)^{-4/5} & (\mathrm{FS}) \\ (v_w - v_{fs})^2 \approx 120\ \mathrm{keV}\ v_{w,9}^2 & (\mathrm{WTS}) \\ (v_j - v_{fs})^2 \approx 17\ \mathrm{MeV}\left(\dfrac{v_j}{0.3c}\right)^2 & (\mathrm{JTS}). \end{cases} \tag{9}$$

The corresponding cooling timescale of the post-shock thermal plasma is given by (e.g., Vlasov et al. 2016)

$$t_{cool} \simeq \frac{3\bar{E}}{2 n_s \mu \Lambda[T_s]} \tag{10}$$

where $n_s = 4\rho_s/\mu m_p$ is the post-shock density assuming strong shocks, and an adiabatic index $\hat{\gamma} = 5/3$. We adopt a cooling function appropriate for solar-metallicity gas, which includes both free–free emission and atomic lines $\Lambda[T_s] = \Lambda_{ff}[T_s] + \Lambda_{line}[T_s]$, where (Schure et al. 2009; Draine 2011),

$$\Lambda_{ff}[T_s] \simeq 3 \times 10^{-27}(T_s/\mathrm{K})^{0.5}\ \mathrm{erg\ s^{-1}\ cm^3}, \tag{11a}$$

$$\Lambda_{lines}[T_s] \simeq 2.8 \times 10^{-18}(T_s/\mathrm{K})^{-0.7}\ \mathrm{erg\ s^{-1}\ cm^3}. \tag{11b}$$

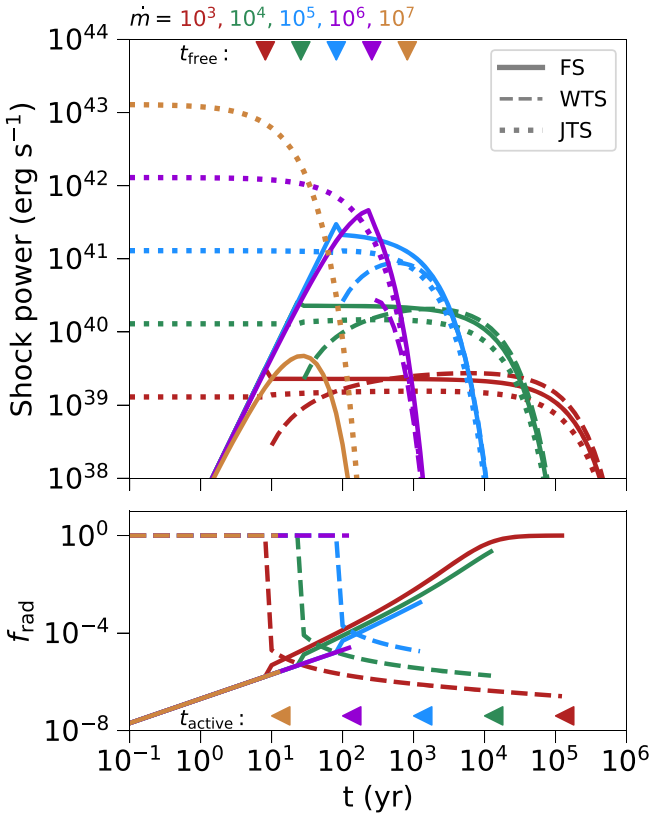

Figure 1. Solid, dashed, and dotted curves show the properties of the forward shock, wind termination shock, and jet termination shock, respectively. The colors denote different accretion rates. The time evolution of the shock power (Equation (8)) is shown in the top panel, and the bottom panel shows the shocks' radiative efficiency (Equation (12)). The left-facing triangles at the bottom frame denote the active lifetime of the accreting engine (Equation (1)), and the downward-facing triangles at the top frame denote the free-expansion timescale of the shock (Equation (2)).

The radiative efficiency of the shocks can be quantified by the parameter (Vlasov et al. 2016; Sridhar & Metzger 2022)

$$f_{\rm rad} = \left(1 + \frac{5}{2}\frac{t_{\rm cool}}{t_{\rm exp}}\right)^{-1}, \tag{12}$$

where $f_{\rm rad} \ll 1 (\simeq 1)$ defines an adiabatic (radiative) shock, respectively.

The top panel of Figure 1 shows the time evolution of the power in the three shocks, for different values of $\dot{m}$. For purposes of calculating the temporal evolution of various shock properties, the engine is smoothly *turned-off* at a time $t = t_{\rm active}$ when accretion stops (Equation (1)), by multiplying the shock properties with an exponential function of the form $e^{-t/t_{\rm active}}$. At early times ($t \ll t_{\rm free}$), the power in the JTS dominates and remains nearly constant (as $v_{\rm j} \gg v_{\rm w} \gtrsim v_{\rm fs}$) until the engine shuts off. Once the shell crosses the free-expansion phase at $t > t_{\rm free}$ (as occurs only for $\dot{m} < 10^6$), the higher $\rho_{\rm fs}$ ($> \rho_{\rm wts} \gg \rho_{\rm jts}$) renders the kinetic power of the FS and WTS comparable to that of the JTS. The bottom panel of Figure 1 shows the radiative efficiency ($f_{\rm rad}$) of the FS and WTS. (We do not show $f_{\rm rad}$ for the JTS because the cooling time of the relativistic particles is extremely long $>10^{10}$ yr, and hence, $f_{\rm rad} \ll 10^{-8}$.) The radiative efficiency of the FS and WTS generally increases with $\dot{m}$. However, unlike the FS, which turns from being adiabatic to radiative after a critical time $t = t_{\rm rad}^{\rm fs}$, the WTS turns from being radiative to adiabatic soon after its onset. Also note that only for $\dot{m} \lesssim 10^4$ does the FS become radiative during the accretion active time $t < t_{\rm active}$.

For the rest of this paper, we shall focus on the JTS, for the following reason, motivated further in the sections to follow. Even though the total energy carried dissipated at the FS dominates that of either the JTS or the WTS, the JTS dominates the shock energy along the narrow solid angle along the jet axis relevant for photohadronic interactions within the geometrically beamed X-ray emission of the accretion flow (see Equation (16) for further discussion).

The magnetic field strength in the vicinity of the JTS can be estimated from the jet magnetization,

$$B_{\rm jts} = \sqrt{16\pi\sigma_{\rm j} m_{\rm p} n_{\rm s} v_{\rm j}^2} \approx 4\ {\rm mG}\ \sigma_{\rm j,-1}^{1/2}\left(\frac{v_{\rm j}}{0.3c}\right)^{1/2}\eta_{-1}^{1/2} \times \begin{cases} \dot{m}_5^{1/2}\left(\dfrac{t}{80\ {\rm yr}}\right)^{-1} & (t < t_{\rm free}) \\ \dot{m}_5^{3/10} v_{\rm w,9}^{3/5} n_1^{1/5}\left(\dfrac{t}{80\ {\rm yr}}\right)^{-3/5} & (t > t_{\rm free}), \end{cases} \tag{13}$$

where $n_{\rm s} = 4\rho_{\rm jts}/\mu {\rm m_p}$ is the post-JTS particle number density.

2.2. Background Radiation

There are at least three sources of background photons[8] with which relativistic ions accelerated at the JTS (Section 3.3) can interact to produce neutrinos.

(1) *Disk thermal emission.* For accretion rates $\dot{m} \gg 1$, advection and outflows from the accretion disk limit the bolometric luminosity of the blackbody emission to Begelman et al. (2006), Poutanen et al. (2007),

$$L_{\rm bol} = L_{\rm Edd}(1 + \ln \dot{m}) \approx 10^{40}\ {\rm erg\ s^{-1}}(1 + \ln \dot{m}_5). \tag{14}$$

The isotropic-equivalent luminosity of the disk emission along the axis of the inner accretion funnel, however, can greatly exceed this value due to geometric collimation by the accretion flow (e.g., King 2009). For an X-ray emitting cone of half-opening angle $\theta_{\rm X} \ll 1$, the corresponding beaming fraction can be defined as

$$f_{\rm b,X} \equiv 2\pi[1 - \cos(\theta_{\rm X})]/4\pi \simeq \theta_{\rm X}^2/4. \tag{15}$$

Motivated by radiation magnetohydrodynamical simulations of super-Eddington accretion (Sadowski & Narayan 2015, who found $f_{\rm b,X} \approx 10^{-3}$ for $\dot{m} \sim 10^3$), we conservatively adopt a beaming fraction $f_{\rm b,X} \approx 10^{-3}(\dot{m}/10^3)^{-1}$, shallower than the $f_{\rm b,X} \propto \dot{m}^{-2}$ dependence advocated by King (2009). This gives an isotropic-equivalent X-ray luminosity (within angles $\theta < \theta_{\rm X}$),

$$L_{\rm X} = \frac{L_{\rm bol}}{f_{\rm b,X}} \approx 10^{45}\ {\rm erg\ s^{-1}}(1 + \ln \dot{m}_5)\dot{m}_5. \tag{16}$$

The high densities of the jetted outflows permeating the collimated accreting funnel further imply that thermal photons

[8] We do not consider thermal synchrotron radiation that peaks in the radio band (Sridhar & Metzger 2022) because the required proton threshold energy of $E_{\rm thr} \sim 10$ ZeV to interact with ~GHz photons and produce pions (Equation (23)) is much larger than the maximum energy to which protons can be accelerated at the hypernebula JTS (Figure 5).

emerge not directly from the disk surface, but rather from the fast wind and/or jet photosphere at much larger radii. Assuming the kinetic luminosity of the fast wind to be comparable to its photon luminosity (Sadowski & Narayan 2015), i.e., $\dot{M}_j v_j^2/2 \approx L_X$, the photosphere radius can be approximated as

$$r_{ph} = \frac{L_X \sigma_T (1 - v_j/c)}{4\pi m_p c^2 v_j} \approx 10^{12}\,\mathrm{cm}(1 + \ln \dot{m}_5)\dot{m}_5 \left(\frac{v_j}{0.3c}\right)^{-1}, \tag{17}$$

where σ_T is the Thomson cross section. The resulting effective temperature of the thermal emission is given by

$$k_B T_{eff} = \left(\frac{L_X}{4\pi r_{ph}^2 \sigma_{SB}}\right)^{1/4} \approx 60\ \mathrm{eV} \times (1 + \ln \dot{m}_5)^{-1/4} \dot{m}_5^{-1/4} \left(\frac{v_j}{0.3c}\right)^{1/2}, \tag{18}$$

where $\sigma_{SB} = 5.67 \times 10^{-5}\ \mathrm{g\ s^{-3}\ K^{-4}}$ is the Stefan-Boltzmann constant. Interestingly, hypernebulae could thus manifest as ultraluminous supersoft X-ray sources (Kahabka 2006; Mićić et al. 2022).

The number density of the thermal disk photons at the radius of the JTS is thus given by

$$n_X^{th} \approx \frac{L_X}{4\pi R^2 k_B T_{eff} c} = 4 \times 10^6\,\mathrm{cm^{-3}}(1 + \ln \dot{m}_5)^{5/4} \dot{m}_5^{5/4} \times \left(\frac{v_j}{0.3c}\right)^{-1/2} \times \begin{cases} v_{w,9}^{-2}\left(\frac{t}{80\ \mathrm{yr}}\right)^{-2} & (t < t_{free}) \\ \left(\frac{L_{w,42}}{n_1}\right)^{-2/5}\left(\frac{t}{80\ \mathrm{yr}}\right)^{-6/5} & (t > t_{free}) \end{cases}. \tag{19}$$

(2) *Disk-corona Comptonized nonthermal emission.* The thermal UV and/or X-ray disk emission may be up-scattered by a Comptonizing corona. Given the large Thomson depth in the polar funnel, the Comptonized nonthermal emission would be generated in the funnel/jet walls at large distances $> r_{ph}$ (e.g., powered by processes such as magnetic reconnection Sironi & Beloborodov 2020; Sridhar et al. 2021b, 2023) along the jet boundary (Ripperda et al. 2020). The Comptonized photons follow a power-law spectrum $N(\epsilon) \propto \epsilon^{-q}$ with say, a power-law index $q = 2$, from the thermal peak energy $\epsilon_{pk,th}^{eff} = 3k_B T_{eff}$ to the pair creation threshold energy $2m_e c^2$ (Svensson 1987). Assuming that the energy contained in the nonthermal photons is comparable to the thermal photons, the number density of the nonthermal photons can be estimated as

$$n_X^{nth} \sim \frac{L_X}{4\pi R^2 \epsilon_{pk,th}^{eff} c \ln(2m_e c^2/\epsilon_{pk,th}^{eff})} \approx 4 \times 10^5\,\mathrm{cm^{-3}}\left(\frac{v_j}{0.3c}\right)^{-1/2}(1 + \ln \dot{m}_5)^{5/4}\dot{m}_5^{5/4} \times \begin{cases} v_{w,9}^{-2}\left(\frac{t}{80\ \mathrm{yr}}\right)^{-2} & (t < t_{free}) \\ \left(\frac{L_{w,42}}{n_1}\right)^{-2/5}\left(\frac{t}{80\ \mathrm{yr}}\right)^{-6/5} & (t > t_{free}) \end{cases}. \tag{20}$$

(3) *Free–Free X-ray emission.* The FS becomes radiative after a time $t > t_{rad}^{fs}$ when $f_{rad} \simeq 1$ (see bottom panel of Figure 1), and its luminosity dominates that of both the WTS and JTS, which remain adiabatic. The number density of photons near the FS can be estimated as

$$n_X^{ff} = \frac{\Lambda_{ff}}{\Lambda} \frac{f_{rad} L_s}{4\pi R^2 \bar{E} c}, \tag{21}$$

where the factor Λ_{ff}/Λ accounts for the fraction of the FS's total luminosity radiated via free–free emission, which typically dominates over line cooling given the high post-shock temperature $T > 10^7$ K (Equation 9).

The photon number densities from the aforementioned three emission processes are shown in Figure 2. Although n_X^{ff} increases with time as $\propto t^{4/5}$ whereas n_X^{th} and n_X^{nth} decreases as $\propto t^{-6/5}$, we find $n_X^{th} > n_X^{nth} \gg n_X^{ff}$ at all times $t < t_{active}$ for all $\dot{m}$. Thus motivated, in what follows, we shall focus on the interaction of ions accelerated at the JTS with the thermal disk emission and its nonthermal Comptonized counterpart. The densities of the other sources of hard X-ray and/or gamma-ray photons, e.g., from the jet knots (Safi-Harb et al. 2022) are also negligible compared to $n_X^{th/nth}$.

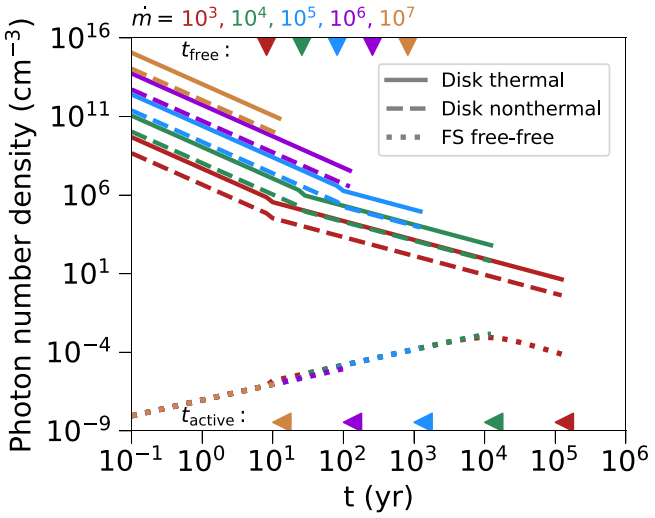

Figure 2. Background UV/X-ray photon number density near the location of the JTS. Solid curves represent the disk blackbody photons (Equation (19)), dashed curves represent the Compton upscattered nonthermal photons (Equation (20)), and the dotted curves represent the free–free X-ray photons (Equation (21)). Different colors indicate different accretion rates. The left-facing triangles in the lower frame represent the active duration of the engine (t_{active}; Equation (1)) for different $\dot{m}$, and the bottom-facing triangles along the upper frame mark the end of the free expansion of the shell (t_{free}; Equation (2)).

3. Model for Neutrino Emission

3.1. Pion Production

Immersed in an UV/X-ray photon field (Section 2.2), the protons accelerated at the JTS can engage in the photomeson process through the Δ^+-resonance (Berezinskii et al. 1990),

$$p + \gamma \longrightarrow \Delta^+ \longrightarrow \begin{cases} p + \pi^0 \\ n + \pi^+ \end{cases}. \tag{22}$$

The Δ^+-resonance decay branching ratio is such that two-thirds of the products follow the neutral pion (π^0) channel, and the remaining one-third will follow the charged pion (π^+) channel. The pion production through the photohadronic process (Equation (22)) with thermal photons from the accretion disk

peaks at the Δ^+-resonance at a threshold proton energy given by Mannheim & Biermann (1989), Waxman & Bahcall (1997),

$$E_{\rm thr} \gtrsim \frac{E_{\Delta^+}}{k_{\rm B}T_{\rm eff}}\frac{m_{\rm p}c^2}{2} \approx 2\ {\rm PeV}(1+\ln\dot{m}_5)^{1/4}\dot{m}_5^{1/4}\left(\frac{v_{\rm j}}{0.3c}\right)^{-1/2}, \quad (23)$$

where $E_{\Delta^+} \approx 0.3$ GeV is the energy where the cross section peaks. However, note that $E_{\rm thr}$ can be smaller by a factor $(\epsilon/2m_{\rm e}c^2)^{-2}$ for photohadronic interactions with higher-energy nonthermal photons with energies $k_{\rm B}T_{\rm eff} < \epsilon < 2m_{\rm e}c^2$ (more discussion around Equation (37)). Since $E_{\rm thr} \gg \bar{E}$, the photohadronic reactions with thermal photons can proceed only with the JTS-accelerated protons from the nonthermal tail with energies $E \gg \bar{E}$ (more in Section 3.3).

In addition to this channel, pions will also be produced through *pp*-interactions that follow

$$p + p \longrightarrow \begin{cases} \pi^+ + X \\ \pi^0 + X \\ \pi^- + X \end{cases} \quad (24)$$

where X refers to any other by-products (such as ϕ-mesons, K-mesons, pions, protons, and neutrons) produced in the reaction other than the particle indicated. In the following section, we calculate the particle interaction timescales that will determine the efficiency of pion production through $p\gamma$ (Equation (22)) and *pp* channels (Equation (24)).

3.2. Particle Interaction Timescales

The most energetic particles will propagate inside the magenetized region of the hypernebula on the light-crossing time, $t_{\rm cross} = R/c$, while most of the less-energetic particles that are trapped inside the nebula by the turbulent magnetic field would escape the system on a longer, shell expansion timescale (Equation (5)). The particles that are the most relevant for neutrino production are the ones that are trapped within the X-ray solid angle (Equation (15)) and can engage in photohadronic interactions. We can correspondingly define a timescale for laterally crossing the X-ray cone as

$$t_{\rm cross}^{\rm cone} \simeq \frac{R}{v_{\rm fs}}\theta_{\rm X} \approx 0.5\ {\rm yr}\left(\frac{t}{80\ {\rm yr}}\right)\dot{m}_5^{-1}. \quad (25)$$

Let us first consider the photohadronic interactions of the protons accelerated at the JTS with the thermal and nonthermal photons (Equations (19) and (20)). We can define an optical depth for this interaction, $\tau_{\rm p\gamma}^{\rm (th,nth)} = \sigma_{\rm p\gamma}\kappa_{\rm p\gamma}Rn_{\rm X}^{\rm (th,nth)}$ where, $\sigma_{\rm p\gamma} \sim 5\times10^{-28}\,{\rm cm}^2$ is the cross section of the photopion production (Eidelman et al. 2004) at the Δ^+-resonance, and $\kappa_{\rm p\gamma} \sim 0.15$ is the average fraction of energy lost from a proton per elastic collision. This can be deemed the photopion production efficiency: i.e., the fraction of the shock-accelerated protons that will be converted into pions before streaming out of the shock, so long as they satisfy the threshold energy requirements (Equation (23)).

The corresponding $p\gamma$ interaction timescale is

$$t_{\rm p\gamma}^{\rm (th,nth)} = \frac{t_{\rm cross}^{\rm cone}}{\tau_{\rm p\gamma}^{\rm (th,nth)}} \approx 8(1+\ln\dot{m}_5)^{-5/4}\dot{m}_5^{-7/4}\left(\frac{v_{\rm j}}{0.3c}\right)^{1/2} \times \begin{cases} (10^2,\,10^3)\,{\rm yr}\ v_{\rm w,9}\left(\frac{t}{80\ {\rm yr}}\right)^2 & (t < t_{\rm free}) \\ (10^2,\,10^3)\,{\rm yr}\left(\frac{L_{\rm w,42}}{n_1}\right)^{1/5}\left(\frac{t}{80\ {\rm yr}}\right)^{8/5} & (t > t_{\rm free}) \end{cases}. \quad (26)$$

The other relevant channel of neutrino production is the hadronuclear (*pp*) interaction of protons accelerated by the JTS, whose interaction timescale is

$$t_{\rm pp} \simeq \frac{\theta_{\rm X}}{n_{\rm p}\sigma_{\rm pp}\kappa_{\rm pp}v_{\rm fs}} \approx 1.5\times10^5\ {\rm yr} \times \begin{cases} \dot{m}_5^{-3/2}v_{\rm w}^2\left(\frac{t}{80\ {\rm yr}}\right)^2 & (t < t_{\rm free}) \\ \dot{m}_5^{-1/2}\left(\frac{L_{\rm w,42}}{n_1}\right)^{-1/5}n_1^{-1}\left(\frac{t}{80\ {\rm yr}}\right)^{2/5} & (t > t_{\rm free}), \end{cases} \quad (27)$$

where $\sigma_{\rm pp} \sim 10^{-25}\,{\rm cm}^{-2}$ (at $\sim$1 EeV) and $\kappa_{\rm pp} \sim 0.5$ (Eidelman et al. 2004). Note that $t_{\rm pp}$ increases sharply as $\propto t^2$ only until $t = t_{\rm free}$, beyond which it increases moderately as $\propto t^{2/5}$, given now the constant influx of protons into the shell from the CSM (see Equation (7)). The total pion creation rate due to photopion and hadronuclear interactions can be written as

$$1/t_{\pi,\rm cre} = 1/t_{\rm p\gamma}^{\rm th} + 1/t_{\rm p\gamma}^{\rm nth} + 1/t_{\rm pp}. \quad (28)$$

The top panel of Figure 3 shows the aforementioned interaction timescales for different accretion rates ($\dot{m} = 10^3$, dotted curves; $\dot{m} = 10^5$, solid curves; and $\dot{m} = 10^7$, dashed curves). At all times, for all choices of $\dot{m}$, $t_{\rm cross} < t_{\rm exp}$. However, $t_{\rm cross}^{\rm cone}$ is dependent on $\dot{m}$ through the beaming fraction (Equation (15)): $t_{\rm cross}^{\rm cone} < t_{\rm cross}$ for $\dot{m} \gtrsim 10^4$. For low $\dot{m} \sim 10^3$ systems, the timescales follow the hierarchy, $t_{\rm exp} \ll t_{\rm p\gamma}^{\rm th} < t_{\rm p\gamma}^{\rm nth} < t_{\rm pp}$ at earlier times $t \lesssim t_{\rm free}$, and at later times $t \gg t_{\rm free}$, the constant shell density changes the hierarchy to $t_{\rm pp} < t_{\rm p\gamma}^{\rm th} < t_{\rm p\gamma}^{\rm nth}$. For higher $\dot{m} \sim 10^7$ cases, the timescale hierarchy obeys $t_{\rm p\gamma}^{\rm th} < t_{\rm p\gamma}^{\rm nth} < t_{\rm cross} < t_{\rm pp} < t_{\rm exp}$ during most of their lifetimes. Overall, (although not shown in Figure 3), $t_{\pi,cre}$ overlaps with $t_{\rm p\gamma}^{\rm th}$ at earlier times and with $t_{\rm pp}$ at later times (if applicable, e.g., for low $\dot{m} \sim 10^3$ cases).

Pion production happens efficiently as long as $t_{\pi,\rm cre}$ is smaller than both the $t_{\rm exp}$ and the synchrotron cooling timescale of the proton given by

$$t_{\rm p,syn} = \frac{6m_{\rm p}^3c}{\sigma_{\rm T}m_{\rm e}^2\bar{\gamma}_{\rm p}B_{\rm sh}^2} \sim 10^{10}\ {\rm yr}\ \sigma_{\rm j,-1}^{-1}\left(\frac{v_{\rm j}}{0.3c}\right)^{-1}\eta_{-1}^{-1} \times \begin{cases} \dot{m}_5^{-1}\left(\frac{t}{80\ {\rm yr}}\right)^2 & (t < t_{\rm free}) \\ \dot{m}_5^{-3/5}v_{\rm w,9}^{-6/5}n_1^{-2/5}\left(\frac{t}{80\ {\rm yr}}\right)^{6/5} & (t > t_{\rm free}) \end{cases} \quad (29)$$

where we take $\bar{\gamma}_{\rm p} \sim 10^6$ to be the average Lorentz factor of the accelerated protons with energy in the relevant energy range for

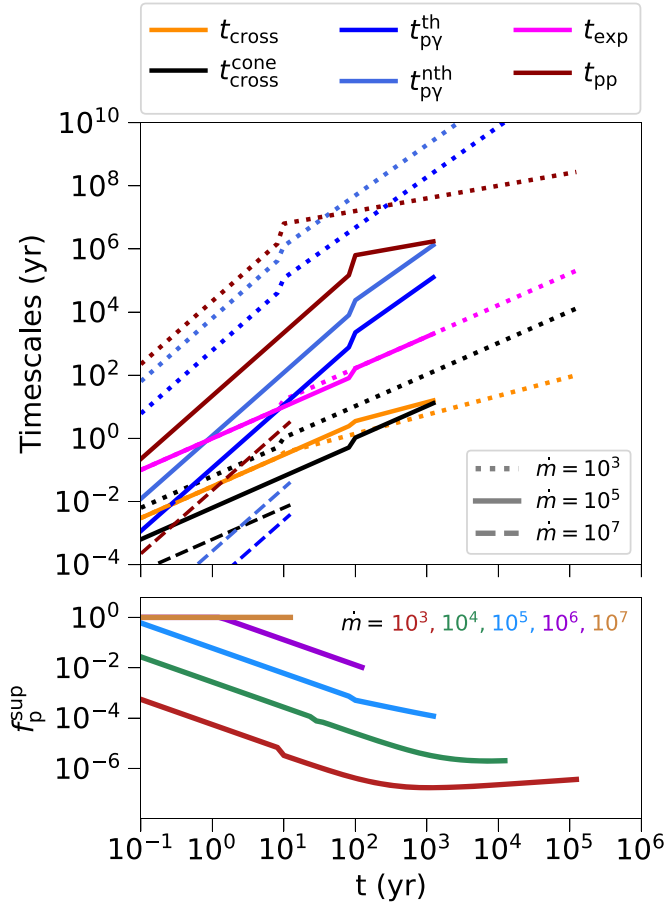

Figure 3. Top panel: Different timescales of the system for our fiducial model with $\dot{m} = 10^5$ (solid curves); dotted and dashed curves represent $\dot{m} = 10^3$, and $\dot{m} = 10^7$, respectively. Pink curves denote the hypernebula expansion timescale (Equation (5)); yellow curves denote the light-crossing timescale of the hypernebula ($t_{\rm cross} = R/c$), and the black curves denote the time particles take to laterally cross the X-ray emission cone (Equation (25)). Dark and light blue curves denote the interaction timescale of protons between thermal and nonthermal photons (Equation (26)), respectively. Dark brown curves denote the hadronic (pp) interaction timescale (Equation (27)). The overall pion creation timescale (Equation (28)), not shown here, overlaps with $t^{\rm th}_{\rm p\gamma}$ at earlier times, and with $t_{\rm pp}$ at later times, when applicable (e.g., for $\dot{m} = 10^3$). Bottom panel: neutrino production suppression factor for different accretion rates for the fiducial model (Equation (30)).

neutrino production ($E_{\rm thr} < E < E_{\rm max}$; more in Equations (35) and (23)). Comparing the curves in the top panel of Figure 3 demonstrates the generally weak impact $t_{\rm p,syn}$ has on any of the relevant timescales for pion production. Given these timescales, the overall efficiency of pion production can be quantified by defining a *suppression factor*,

$$f^{\rm p}_{\rm sup} = \min\left[1, \frac{t_{\rm cross}}{t_{\pi,\rm cre}}, \frac{t^{\rm cone}_{\rm cross}}{t_{\pi,\rm cre}}, \frac{t_{\rm p,syn}}{t_{\pi,\rm cre}}\right]. \quad (30)$$

As the bottom panel of Figure 3 shows, the neutrino production is not suppressed (i.e., $f^{\rm sup}_{\rm p} \sim 1$) for high $\dot{m} \gtrsim 10^6$ systems throughout their lifetimes. This is because of the large background photon density due to a stronger beaming effect that reduces the photohadronic interaction timescales. On the other hand, for weaker accretion rates $\dot{m} \lesssim 10^6$, the pion production efficiency decreases with time as $f^{\rm p}_{\rm sup} \propto t^{-1}$ until $t = t_{\rm free}$ owing to its expansion and smaller background photon density. Soon after, the shell reaches a constant density (leading to a modestly increasing $t_{\rm pp}$), and the consequently decreasing $t_{\rm pp}/t_{\rm exp}$ implies that $t_{\pi,cre}$ becomes dominated by hadronic interactions. This effect is most pronounced for the long-lived $\dot{m} = 10^3$ case where $f^{\rm sup}_{\rm p}$ increases again at later times. Overall, $f^{\rm sup}_{\rm p} \ll 1$ for the majority of the lifetimes of low $\dot{m} \lesssim 10^6$ systems.

An added complication is that pions and muons could suffer synchrotron losses (pion/muon *damping*), which inhibit neutrino production if the former proceeds at a timescale shorter than the latter. We assess this possibility by calculating the critical energy above which their synchrotron losses dominate (Waxman & Bahcall 1998; Metzger et al. 2020),

$$\varepsilon^{\rm syn}_{\pi,\mu} = \left(\frac{6\pi m_{\pi,\mu} c}{\sigma_{\rm T} B^2_{\rm sh} \tau_{\pi,\mu}}\right)^{1/2} \left(\frac{m_{\pi,\mu}}{m_{\rm e}}\right) m_{\pi,\mu} c^2$$
$$\approx (30,\ 2)\,{\rm ZeV}\ \sigma_{\rm j,-1}^{-1/2} \times \left(\frac{v_{\rm j}}{0.3c}\right)^{-1/2} \eta_{-1}^{-1/2}$$
$$\times \begin{cases} \dot{m}_5^{-1/2} \left(\dfrac{t}{80\ {\rm yr}}\right) & (t < t_{\rm free}) \\ \dot{m}_5^{-3/10} v_{\rm w,9}^{-3/5} n_1^{-1/5} \left(\dfrac{t}{80\ {\rm yr}}\right)^{3/5} & (t > t_{\rm free}), \end{cases} \quad (31)$$

where m_π and m_μ are the masses of pions and muons, and $\tau_\pi = 2.6 \times 10^{-8}$ s, and $\tau_\mu = 2.2 \times 10^{-6}$ s are their decay times (Eidelman et al. 2004). These energies—as we show below in Equation (35)—exceed the maximum attainable proton energies during the life of any hypernebula. Therefore, it is fair to assume that majority of the neutrino production from the decay of pions and muons completes before their radiative losses take over. Furthermore, due to the small proton number density at the shock radius (see Equation (7)), the timescales of pion and muon hadronuclear interactions, $t_{\pi,p}$ and $t_{\mu,p}$, greatly exceed their lifetimes τ_π and τ_μ. Therefore, the efficiency of neutrino production is not additionally suppressed.

3.3. Proton Energization

A fraction of the luminosity of the JTS is used to heat protons (to an average energy $\bar{E} \simeq 17$ MeV; Equation (9)) and accelerate them into a power-law distribution of relativistic energies $E \gg \bar{E}$ via the diffusive shock acceleration (DSA) mechanism (Blandford & Ostriker 1978),

$$f_{\rm E} = \begin{cases} 1/2 & (E \sim \bar{E}) \\ \epsilon_{\rm rel} & (E \gg \bar{E}), \end{cases} \quad (32)$$

where $\epsilon_{\rm rel} \lesssim 0.01$ is the efficiency of the nonthermal acceleration process (e.g., for mildly relativistic shocks; Fang et al. 2020).[9] The time evolution of the proton luminosity, $L_{\rm p}(E) = f_{\rm E}(E) L_{\rm s}$, for different $\dot{m}$ is shown in Figure 4.

The accelerated distribution of nonthermal protons can be described by

$$\frac{dN_{\rm p}}{dE} \sim \left(\frac{E}{\bar{E}}\right)^{-q} e^{-E/E_{\rm max}}, \quad (33)$$

[9] Note that nonthermal particle acceleration can be inefficient in highly magnetized shocks (Sironi & Spitkovsky 2011).

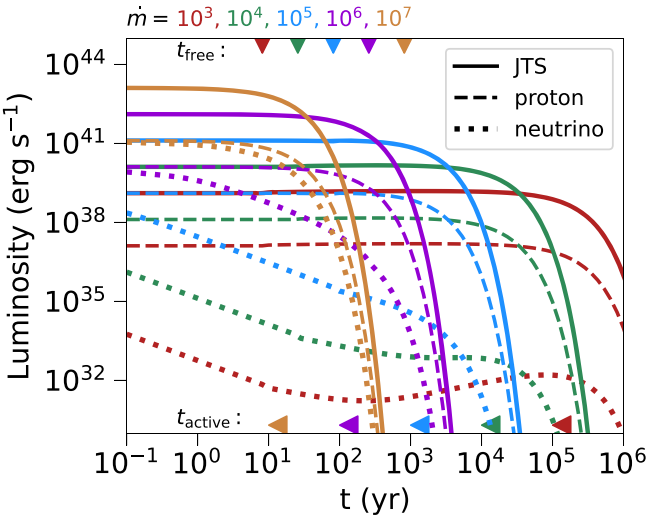

Figure 4. Solid, dashed, and dotted curves show the temporal luminosity evolution of jet termination shock (Equation (8)), and the protons and neutrinos energized there (Equations (32) and (40)), respectively. Different colors represent different accretion rates. The left-facing triangles in the lower frame represent the active duration of the engine ($t_{\rm active}$; Equation (1)) for different $\dot{m}$, and the bottom-facing triangles along the upper frame mark the end of the free expansion of the shell ($t_{\rm free}$; Equation (2)).

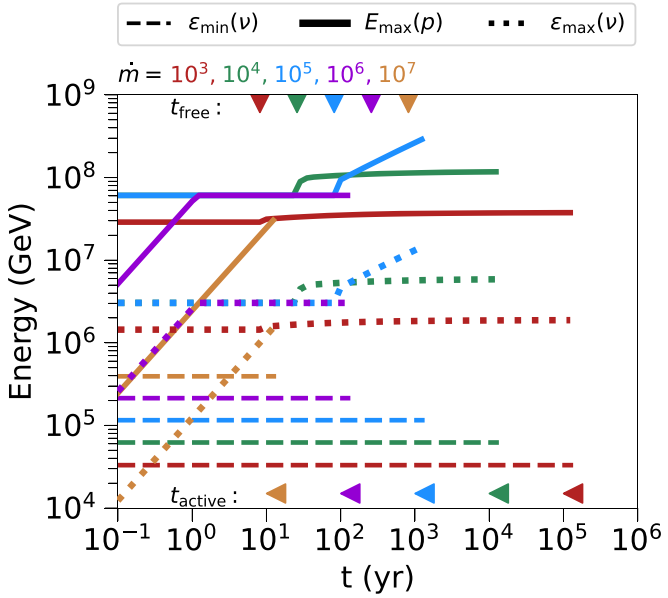

Figure 5. Limitations on the proton and neutrino energies. Solid curves represent the maximum proton energy (Equation (35)); the corresponding maximum attainable neutrino energy is denoted by dotted curves. Dashed curves denote the minimum attainable neutrino energy through the photomeson process (Equation (37)). Different colors represent different accretion rates. The left-facing triangles in the lower frame represent the active duration of the engine ($t_{\rm active}$; Equation (1)) for different $\dot{m}$, and the bottom-facing triangles along the upper frame mark the end of the free expansion of the shell ($t_{\rm free}$; Equation (2)).

where we take $q \simeq 2$ (our fiducial case; Blandford & Eichler 1987); steeper spectra with $q \gtrsim 2$ could also arise as the magnetic fluctuations behind the FS drift away at the local Alfvén speed ("postcursor"; Diesing & Caprioli 2021).

The maximum energy $E_{\rm max}$ attained by the protons in the DSA process is determined by the competition between the diffusive acceleration timescale of particles with Larmor radius $r_{\rm L}$ (e.g., Caprioli & Spitkovsky 2014),

$$t_{\rm acc} \simeq \frac{2}{3}\left(\frac{r_{\rm L}}{c}\right)\left(\frac{v_{\rm j}-v_{\rm fs}}{c}\right)^{-2} = \frac{2Ec}{3eB_{\rm sh}(v_{\rm j}-v_{\rm fs})^2}, \quad (34)$$

and the timescales corresponding to various interaction and cooling processes (e.g., in Figure 3). This yields a maximum ion energy of

$$E_{\rm max} = \frac{3eB_{\rm sh}(v_{\rm j}-v_{\rm fs})^2}{2c}\min\left[t_{\rm cross}, t_{\rm cross}^{\rm cone}, t_{\rm exp}, t_{\rm p\gamma}^{\rm (th,nth)}, t_{\rm pp}\right]. \quad (35)$$

Equation (35) provides a system-size-limited maximum energy of the particles considering that the energized particles with $r_{\rm L} > R$ (and the X-ray cone lateral radius) would escape the accelerator (Hillas 1984) and do not contribute to the neutrino production. The solid curves in Figure 5 show the evolution of $E_{\rm max}(t)$ for different $\dot{m}$—complicated by the influence of the X-ray beaming cone's opening angle on various particle interaction timescales. The highest energy attained in $\dot{m} = 10^3$ and 10^7 cases is $\sim$30 PeV, and the highest energy attained overall is $\sim$300 PeV, in the $\dot{m} = 10^5$ case.

Figure 6 shows example ($q = 2$) snapshots of the proton spectra for different $\dot{m}$, taken at the end of the free-expansion and active phases (times $t_{\rm free}$ and $t_{\rm active}$, respectively).

3.4. Pion Decay to Neutrinos

The pions produced through the $p\gamma$ (Equation (22)) and pp (Equation (24)) channels will eventually decay into neutrinos and gamma rays following

$$\pi^0 \longrightarrow \gamma\gamma; \quad (36a)$$

$$\pi^+ \longrightarrow \mu^+ + \nu_\mu; \quad (36b)$$

$$e^+ + \nu_{\rm e} + \bar{\nu}_\mu; \quad (36c)$$

$$\pi^- \longrightarrow \mu^- + \bar{\nu}_\mu; \quad (36d)$$

$$e^- + \bar{\nu}_{\rm e} + \nu_\mu. \quad (36e)$$

In the absence of significant pion and/or muon damping (Equation (31)), the ratio of the neutrino flavors resulting from pion decay, post-oscillation, is $\nu_{\rm e}:\nu_\mu:\nu_\tau = 1:1:1$ by the time they reach Earth (Becker 2008).

Let us now consider the photomesonic process with thermal background photons, where the produced pions decay into neutrinos with $\sim$5% of the proton's energy $\varepsilon \approx E/20$ (Stecker 1968; Kelner & Aharonian 2008). This sets the lowest attainable neutrino energy to be

$$\varepsilon_{\rm min} \approx \max[\bar{E}/20, E_{\rm thr}/20]$$
$$\approx 100\ {\rm TeV}(1+\ln\dot{m}_5)^{1/4}\dot{m}_5^{1/4}\left(\frac{v_{\rm j}}{0.3c}\right)^{-1/2}. \quad (37)$$

Note that $\varepsilon_{\rm min}$ can be smaller by a factor $(\epsilon/2m_{\rm e}c^2)^{-2}$ for photohadronic interactions with nonthermal photons with energies $k_{\rm B}T_{\rm eff} < \epsilon < 2m_{\rm e}c^2$. This would effectively place the minimum neutrino energy cutoff at $\varepsilon_{\rm min}\,[\epsilon_{\rm pk,th}^{\rm eff}/k_{\rm B}T_{\rm eff}]^{-2} \sim$ 10 TeV (see Equation (23) and also Section 2.2(2)). The production of even lower-energy neutrinos mediated by interactions with nonthermal photons of energies $\epsilon > \epsilon_{\rm pk,th}^{\rm eff}$ is highly suppressed. On the other hand, the absolute maximum neutrino energy as set by the accelerator is $\varepsilon_{\rm max} \sim E_{\rm max}/20$.

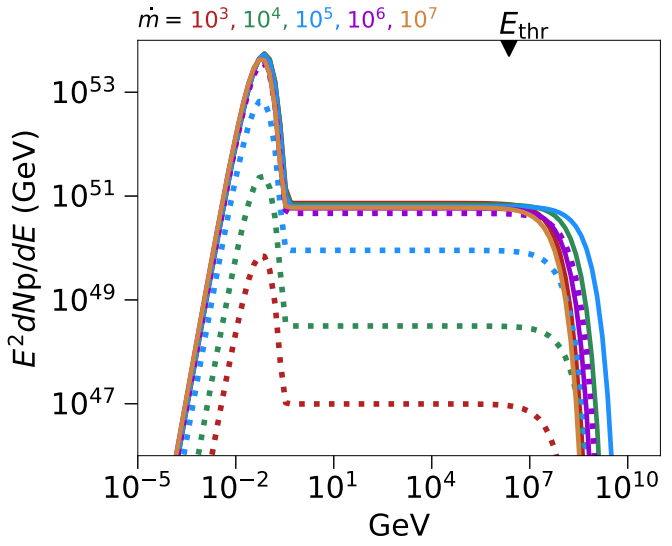

Figure 6. Energy spectra of protons energized at the JTS. Solid curves are at $t = t_{\rm active}$ (Equation (1)), and the dotted curves are at an earlier time, $t = t_{\rm free}$ (Equation (2)). Different colors indicate different accretion rates. The threshold energy to produce neutrinos via photohadronic interaction with thermal background photons ($E_{\rm thr}$; Equation (23)) is indicated along the top frame of the figure.

Figure 5 shows $\varepsilon_{\rm min}$ as the horizontal dashed line, which is independent of the age of the hypernebula, and cares only about $k_{\rm B}T_{\rm eff}$ through $\dot{m}$ (Equation (18)). $\varepsilon_{\rm max}$ is denoted by dotted curves, which trace $E_{\rm max}$ with a scaling offset of $1/20$. In general, hypernebulae generate neutrinos throughout their lifetime. An exception to this are the high $\dot{m} > 10^7$ systems where their short lifetimes (and therefore, a smaller acceleration region) restrict $E_{\rm max} < \varepsilon_{\rm min}$ and prevent any neutrino production.

The neutrino luminosities from the JTS-accelerated $p\gamma$ and pp interactions are

$$L_\nu^{\rm p\gamma} = \frac{3}{8} f_{\rm p\gamma} L_{\rm p} = \frac{27\pi}{64} f_{\rm p\gamma} f_{\rm E} R^2 \rho_{\rm jts} (v_{\rm j} - v_{\rm fs})^3; \quad (38a)$$

$$L_\nu^{\rm pp} = \frac{1}{2} f_{\rm pp} L_{\rm p} = \frac{9\pi}{16} f_{\rm pp} f_{\rm E} R^2 \rho_{\rm jts} (v_{\rm j} - v_{\rm fs})^3; \quad (38b)$$

where the neutrino conversion efficiency factors are

$$f_{\rm p\gamma}^{\rm (th,nth)} = 1 - e^{-\tau_{\rm p\gamma}} = 1 - e^{-t_{\rm cross}^{\rm cone}/t_{\rm p\gamma}^{\rm (th,nth)}}; \quad (39a)$$

$$f_{\rm pp} = 1 - e^{-\tau_{\rm pp}} = 1 - e^{-t_{\rm cross}^{\rm cone}/t_{\rm pp}}. \quad (39b)$$

The factor $3/8$ in Equation (38a) accounts for the fraction of the proton energy that goes into neutrino products (Waxman & Bahcall 1997; Fang & Metzger 2017), i.e., charged pions are produced in a $p\gamma$ interaction only half the time on average, and when a pion decays, $\sim 3/4$ of its energy goes to neutrinos (see Equations (21) and (36a)). The factor $1/2$ in Equation (38a) accounts for the fact that pions are produced with $\sim 2/3$ probability in a pp interaction (see Equation (24)), and $\sim 3/4$ of their energy is carried away by neutrinos. Finally, each hypernebula provides a total neutrino energy flux per flavor that follows the proton energy spectrum at a given time as

$$E_\nu^2 \frac{dN_\nu}{dE_\nu} = \frac{E_{\rm p}^2}{2} \frac{dN_{\rm p}}{dE} \left[\frac{3}{4} f_{\rm p\gamma}^{\rm (th,nth)} + f_{\rm pp} \right]. \quad (40)$$

Note that, in the calculation above for the neutrino luminosity and its flux, we assume for simplicity that the opening angle of the JTS ($\theta_{\rm j}$) is comparable to that of the X-ray cone ($\theta_{\rm X}$; Equation (15)). On the other hand, one can expect a scenario where $\theta_{\rm X} > \theta_{\rm j}$, and that the precessing X-ray cone irradiates different patches of the JTS at different times. In such a case, the effective expansion time (e.g., see Equation (25)) could be lower by a factor $(\theta_{\rm X}/\theta_{\rm j})^2$. This ratio can be estimated through magnetohydrodynamic simulations of advection-dominated hyper-Eddington accretion disks, and is beyond the scope of this work.

4. Observational Implications

4.1. Luminosity and Volumetric Rates

Figure 4 shows the combined $L_\nu^{\rm p\gamma} + L_\nu^{\rm pp}$ neutrino *light curves* for different $\dot{m}$. The neutrino luminosity closely follows the profile of the JTS and proton luminosity for $\dot{m} = 10^7$ case, but it evolves as $\propto t^{-1}$ for $\dot{m} \lesssim 10^6$ cases. For even lower $\dot{m} \lesssim 10^4$ cases, the neutrino luminosity increases again before turning off: this is due to the onset of hadronic (pp) channels of neutrino production at later times. The peak neutrino luminosity is larger for higher $\dot{m}$: for the fiducial cases shown in Figure 4, the brightest emission ($L_\nu = 10^{41}\,{\rm erg\,s^{-1}}$) is seen from $\dot{m} = 10^7$ during the early moments of JTS onset.

Whether neutrino emission can be observed from an individual hypernebulae, however, depends on the abundance of such sources in the universe, if the emission is nearly isotropic. The volumetric rate of hypernebulae can be assumed to follow common envelope events involving a black hole and/or neutron star with donor stars more massive than $m_\star = 10$. Schrøder et al. (2020) find this frequency to be $\sim 0.6\%$ core-collapse SN rate, corresponding to a local-universe (redshift $z = 0$) volumetric rate of $\mathcal{R}_0 \sim 10^3\,{\rm Gpc^{-3}\,yr^{-1}}$ (Strolger et al. 2015; Vigna-Gómez et al. 2018). This rate is also in agreement (within an order of magnitude) with that of engine-powered FBOTs ($\mathcal{R}_0 \sim 300\,{\rm Gpc^{-3}\,yr^{-1}}$), which could be failed common envelope events (Coppejans et al. 2020; Metzger 2022; Ho et al. 2023), the occurrence rate of massive-star binaries with mass-transfer rates $\dot{M} \gtrsim \dot{M}_{\rm Edd}$ ($\mathcal{R}_0 \sim 100\,{\rm Gpc^{-3}\,yr^{-1}}$; Pavlovskii et al. 2017), and $\sim 1\%$–10% of all the luminous red novae merger events (Karambelkar et al. 2023). Assuming an active timescale of $\sim 10\,{\rm yr}$ (for the neutrino-brightest $\dot{m} = 10^7$ case), one active hypernebula can be expected within 50 Mpc. In the most optimistic scenario (considering $\eta \sim 1$), the peak neutrino flux from a *local* ($\sim 50\,{\rm Mpc}$) source would be $10^{-10}\,{\rm GeV\,s^{-1}\,cm^{-2}\,sr^{-1}}$, suggesting that the prospects of detecting neutrinos from individual hypernebulae are not encouraging.

However, if the emission is beamed, then the apparent neutrino luminosity of each of the individual sources would be up to $10^{48}\,\dot{m}_7\,{\rm erg\,s^{-1}}$ (also see Figure 4). Assuming a volumetric rate of $\mathcal{R}_0 \sim 300\,{\rm Gpc^{-3}\,yr^{-1}}$ (corresponding to FBOTs), the apparent density of such sources would be $3 \times 10^{-5} \dot{m}_7^{-1}\,{\rm Gpc^{-3}\,yr^{-1}}$. Assuming a detection sensitivity of $\Phi_{\nu_\mu} \sim 3 \times 10^{-12}\,{\rm TeV^{-1}\,cm^{-2}\,s^{-1}}$ at 1 TeV (Aartsen et al. 2020), a source with an E^{-2} spectrum between 10^3 and 10^7 GeV (based on Figure 7) can be observed up to a comoving distance of $\sim 8\,\dot{m}_7^{1/2}$ Gpc, which corresponds to $\sim 0.015\,\dot{m}_7^{1/2}$ source per year. Considering that the emission duration of a $\dot{m} = 10^7$ source is only $\sim 10\,{\rm yr}$, such a rate is consistent with

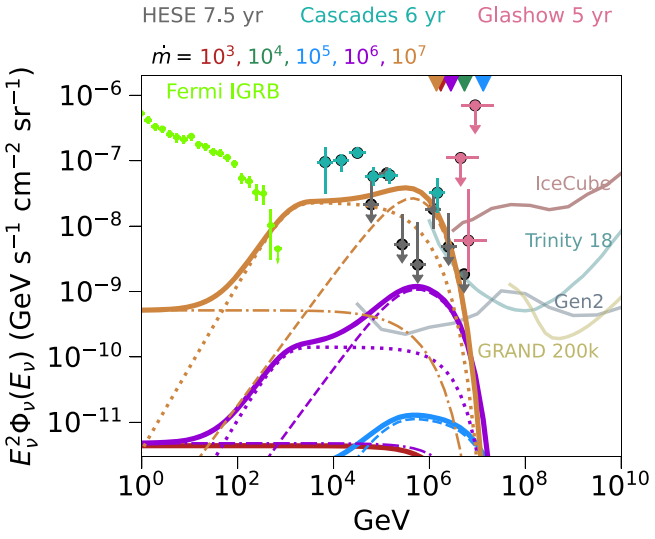

Figure 7. All-flavor HE diffuse background neutrino spectra. The IceCube measurements shown are from the 7.5 yr high-energy starting event sample (gray markers; Abbasi et al. 2021), 6 yr high-energy cascades (turquoise markers; Aartsen et al. 2020), and the 5 yr Glashow resonance (pink markers; IceCube Collaboration et al. 2021). For comparison, the Fermi extragalactic isotropic gamma-ray background is shown with green markers (Ackermann et al. 2015). Error bars and upper limits represent 68% confidence intervals. The 10 yr sensitivity limits of current (IceCube, in light maroon, is based on detected neutrino events; Aartsen et al. 2013) and future (Trinity with 18 telescopes, light green; Nepomuk Otte et al. 2019, IceCube-Gen2, gray; IceCube-Gen2 Collaboration et al. 2014; Aartsen et al. 2021, GRAND with 200,000 stations, light gold; Álvarez-Muñiz et al. 2020) neutrino detectors are also provided for comparison. Left panel: Solid curves are the total volume-integrated neutrino flux during the active lifetime of hypernebula obtained for models with different accretion rates (color-coded) but otherwise the same fiducial parameters ($v_w = 0.03c$, $v_j = 0.3c$, $n = 10$, $\sigma_j = 0.1$, $\eta = 0.5$; see Section 2 for more details). Dashed and dotted curves represent the contribution of photomesonic ($p\gamma$) interaction with thermal and nonthermal photons, respectively, and dashed–dotted curves denote the contribution of hadronic interactions (pp). The maximum neutrino energies for different $\dot{m}$ are color-coded and marked as down-facing triangles along the top frame.

the absence of a single hypernebula neutrino source detected by IceCube during its ∼10 yr operation duration.

Recently, IceCube reported a 1 TeV flux of $\simeq 1.5 \times 10^{-7}\,\mathrm{GeV\,s^{-1}\,cm^{-2}}$ from NGC 1068 (at 14.4 Mpc; IceCube Collaboration et al. 2022). The peak flux from a single hypernebula accreting at $\dot{m} = 10^7$ situated at that distance (∼10% chance) would be $2.5 \times 10^{-9}\,\mathrm{GeV\,s^{-1}\,cm^{-2}}$ (see Figure 4). Therefore, the observed neutrino flux from NGC 1068 could, in principle, be explained by a single hypernebula if (1) the JTS is weakly magnetized $\sigma_j \lesssim 10^{-3}$, resulting in a larger $\epsilon_{rel} \sim 0.1$ (Sironi & Spitkovsky 2011), or (2) in a scenario where a cluster of hypernebulae migrate to the AGN core (Secunda et al. 2020), while the previous points (1) and (2) should not necessarily be satisfied in most of the hypernebulae lest they violate the constraints from the diffuse flux. Though, we note that other, more favorable, channels involving AGN coronae could well be operating (Murase et al. 2020; Eichmann et al. 2022; Inoue et al. 2022).

As far as the HE diffuse background neutrino flux is concerned, its overall normalization can be explained by non-relativistic shock-powered transients as long as they obey (Fang et al. 2020)

$$\left(\frac{\mathcal{R}_0}{10^5\,\mathrm{Gpc^{-3}\,yr^{-1}}}\right)\left(\frac{E_{tot}}{5 \times 10^{50}\,\mathrm{erg}}\right)\left(\frac{\epsilon_{rel}}{1\%}\right) \sim 1, \tag{41}$$

where the total output energy is E_{tot}, of which a fraction ϵ_{rel} is directed toward accelerating nonthermal ions (see Equation (32)). While the volumetric rates of hypernebulae are smaller than the suggested value in Equation (41) (which is normalized to that of core-collapse SN; Briel et al. 2022), their longer lifetimes, and steady injection of energy into their surroundings brings the total energy budget of any hypernebula (nearly independent of $\dot{m}$) to

$$E_{tot} \approx \int^{t_{active}} L_w dt \sim 5 \times 10^{52}\,\mathrm{erg}\left(\frac{M_\star}{30\,M_\odot}\right) v_{w,9}^2. \tag{42}$$

This demonstrates that hypernebulae could in principle be a significant portion of the HE diffuse background neutrino flux. We note here that the total energy budget and the volumetric rates of hypernebulae are comparable to hypernovae, which have been considered as possible cosmic ray sources (Chakraborti et al. 2011; Senno et al. 2015). The decades- to centuries-long radio X-ray and other multiwavelength counterparts of hypernebulae (Sridhar & Metzger 2022) can be used to tell them apart from hypernovae through a stacking analysis (akin to, e.g., Abbasi et al. 2023b).

Figure 4 shows that although neutrinos are generated throughout the nebula's lifetime, the spectral properties constantly evolving as the hypernebula expands (see also Figure 6). To calculate a representative neutrino flux for each hypernebula, we calculate the weighted-sum of the flux emitted by each hypernebula (Equation (40)) over its lifetime. The integrated observed neutrino flux contributed by all hypernebulae from different redshifts, taking into account the energy loss due to cosmological expansion, can be written as

$$E_\nu^2\Phi_\nu(E_\nu) = \frac{\mathcal{R}_0}{4\pi}\int_0^6 dz \frac{c}{(1+z)^2 H(z)} f(z)\left(E_\nu'^2 \frac{dN_\nu}{dE_\nu'}\right)(z), \tag{43}$$

where $H(z) = H_0[\Omega_m(1+z)^3 + \Omega_\Lambda]^{1/2}$ is the Hubble constant at redshift z, where we take $H_0 \simeq 70\,\mathrm{km\,s^{-1}\,Mpc^{-1}}$, $\Omega_m = 0.315$, and $\Omega_\Lambda = 0.7$ (for a ΛCDM flat cosmology; Planck Collaboration et al. 2020). $E_\nu' = E_\nu(1+z)$ is the redshifted neutrino energy; $f(z) = \mathcal{R}(z)/\mathcal{R}_0$ captures the possibly different volumetric rates of the source at different redshifts. We assume $\mathcal{R}(z=0) \sim 10^3\,\mathrm{Gpc^{-3}\,yr^{-1}}$, and that $\mathcal{R}$ follows star formation history. This lets us obtain $f(z)$ using the following empirical fit (reliable upto $z \sim 6$) of Strolger et al. (2004):

$$f(z) = \frac{a[t^b e^{-t/c} + de^{d(t-t_0)/c}]}{de^{-dt_0/c}}, \tag{44}$$

where $a = 0.182$, $b = 1.26$, $c = 1.865$, $d = 0.071$, $t = 1/H_0(1+z)$ is the look-back time, and $t_0 = 1/H_0 \sim 14$ Gyr is the age of the universe. Since the volumetric rate of hypernebulae scales as the star formation history ($f(z)$, which increases with redshift), the total number of hypernebulae contributing to the neutrino flux is ∼10 ×, what one would get if a constant $\mathcal{R} = \mathcal{R}_0$ is assumed.

4.2. Diffuse Neutrino Flux

The left panel of Figure 7 shows the time-averaged, volume-integrated (Equation (43)) neutrino flux energy distribution for

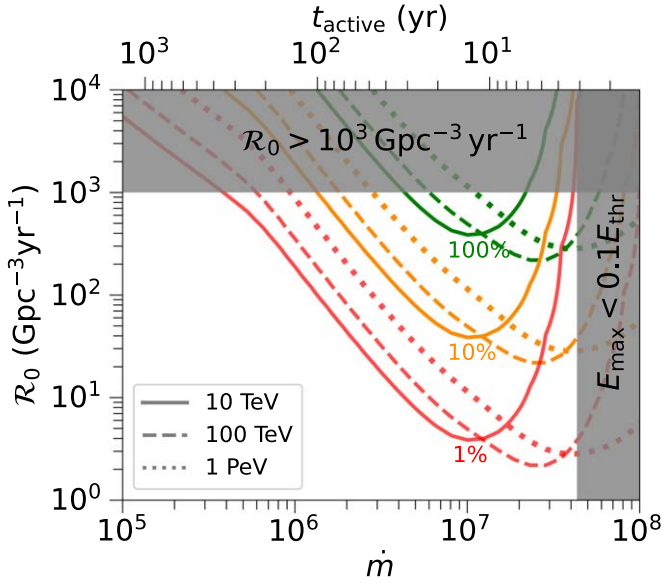

Figure 8. Neutrino flux for a range of volumetric rates $\mathcal{R}_0$ (y-axis) from accretion-powered-hypernebulae with different $\dot{m}$ (bottom x-axis), with other parameters following our '*best fit*' (see Section 4.2, and Appendix C); the top x-axis denotes the active timescale (Equation (1)) for a given $\dot{m}$. The solid, dashed and dotted curves represent the model fluxes in 10 TeV, 100 TeV, and 1 PeV, normalized to the observed fluxes of 10^{-7}, 4×10^{-8}, and 2×10^{-8} GeV s^{-1} cm^{-2} sr^{-1}, respectively. Red, yellow, and green contours denote the parameter space that can supply 1%, 10%, and 100% of the observed flux. The top gray region denotes the parameter space excluded based on the volumetric rate constraint of $\mathcal{R}_0 \lesssim 10^3$ Gpc^{-3} yr^{-3} set by the rate of common envelope events involving compact objects (Schrøder et al. 2020). The right gray region is excluded because extreme $\dot{m}$ events fail to produce neutrinos as their maximum proton energies ($E_{\rm max}$; Equation (35)) are less than the minimum required proton energy to produce neutrinos upon interaction with even the higher-energy nonthermal photons (Equation (23)).

different mass-transfer rates $\dot{m}$ (denoted by different colors). The individual processes contributing to the total flux are shown with different linestyles, i.e., the dominant $p\gamma$ photomesonic reactions with thermal and nonthermal background photons, and the highly subdominant hadronic pp reactions, whose contribution to the neutrino flux is relevant only at lower-energies $<$100 GeV. Also shown for comparison are the observed HE diffuse background neutrino flux (Aartsen et al. 2020), the Fermi/LAT IGRB (Ackermann et al. 2015; circular markers with error bars), and the 10 yr sensitivity limit of future HE and UHE neutrino observatories.

The neutrino spectral peak is primarily determined by the $p\gamma$ interactions with the high-density thermal photons. The HE cutoff is set by the system parameters, independent of the neutrino production channel (Equation (35) and Figure 5). On the other hand, the low-energy turnovers are set by the three different neutrino production channels: the turnovers at $\sim$100 and $\sim$10 TeV are due to the $p\gamma$ interactions with the thermal and nonthermal photons, respectively (see discussion following Equation (37)). The lowest-energy cutoff at $\sim$135 MeV (below the shown energy range of Figure 7) is set by the photohadronic component of the spectrum, at the pion creation threshold energy. The locations of these low-energy turnovers notably depend only weakly on the hypernebula parameters, making them predictive of their neutrino emission (as we demonstrate in Appendix C).

The left panel of Figure 7 shows that if all binaries generate conditions following our high mass-transfer rate model $\dot{m} \sim 10^7$ (brown curve; with otherwise the same fiducial parameters mentioned in Section 2) such systems can in principle explain the entirety of the diffuse 10 TeV to PeV neutrino flux (the chosen parameter combination underestimates the 10 TeV neutrinos, which shall be addressed below with different model parameters). By contrast, the $\dot{m} \sim 10^6$ and $\dot{m} \sim 10^5$ models, acting alone, can supply at most $\sim$1% and $\sim$0.01% of the observed flux, thus ruling out $\dot{m} \ll 10^6$ binaries as significant contributors. Although not visibly shown, the flux in the $\dot{m} \sim 10^3$ case reaches values as high as $\gtrsim 10^{-12}$ GeV s^{-1} cm^{-2} sr^{-1}—comparable to $\dot{m} \sim 10^4$ case—because the long active time of the jet allows pp channel to dominate the waning $p\gamma$ channel for neutrino production.

Appendix C explores a range of models in which the parameters are varied about the fiducial model choices. This exploration yields a *best-fit* model to the diffuse neutrino flux, for the hypernebula parameters $\{\dot{m} = 10^7, v_{\rm w}/c = 0.07, v_{\rm j}/c = 0.17, \eta = 1, n = 1, \sigma_{\rm j} = 1, q = 2\}$. The robust low-energy turnover feature of the model is consistent with the flat/mildly rising nature of the observed neutrino spectrum from 10 to 50 TeV, followed by a broken power law at $\gtrsim$PeV. Though, we present this fit as a proof of principle, we do not intend to suggest that the entire observed diffuse flux is produced by a special population hypernebula; instead, we offer it as a representative of the parameter space around which hypernebulae should occupy, to contribute appreciably to the diffuse flux. Indeed, certain portions of hypernebula parameter space are ruled out because they would overproduce the number of synchrotron-emitting nebula observed by VLASS (e.g., for $v_{\rm j}/c \not> 0.5$; Sridhar & Metzger 2022); our model to the neutrino diffuse background is consistent with this constraint. Our parameter exploration in Appendix C reveals that different parameter combinations can extend the flux cutoff to higher energies, making such systems candidate UHE neutrino sources for upcoming neutrino observatories such as IceCube-Gen2 (IceCube-Gen2 Collaboration et al. 2014; Aartsen et al. 2021), Trinity (Nepomuk Otte et al. 2019), and GRAND (Álvarez-Muñiz et al. 2020). UHE experiments with a sensitivity window well above $\sim$EeV are unlikely to detect these sources.

Above, we have made the assumption that the entire population of hypernebulae is characterized by a single $\dot{m}$, which is an obvious oversimplification. In reality, systems with different $\dot{m}$ will be sampled by nature at different volumetric rates $\mathcal{R}_0$, and even a single binary is likely to span different values of $\dot{m}$ throughout its mass-transfer evolution. We explore this degeneracy further in Figure 8, where the different contours in the $\mathcal{R}_0 - \dot{m}$ space indicate the model neutrino flux at different energies (as a fraction of the observed diffuse flux). We see that the sources with $\dot{m} < 4 \times 10^5$ cannot explain even 1% of the diffuse flux for any realistic occurrence rate $\mathcal{R}_0 \lesssim 10^3$ Gpc^{-3} yr^{-1} (red contours). By contrast, the hypernebula models with $\dot{m} \gtrsim 10^6$ can explain a significant fraction ($\gtrsim$10%; yellow contours) of the observed 10 TeV–1 PeV flux even with a lower local volumetric rate of $\mathcal{R}_0 =$ few $\times$ 100 Gpc^{-3} yr^{-1}. Only $\dot{m} \sim 10^7$ models are able to explain all of the observed flux (green contours). This is relevant because the lives of many binaries may culminate in a highly unstable mass-transfer stage (with $\dot{m} \gtrsim 10^7$), before the compact object plunges into the envelope of the donor star. On the other hand, in a conservative scenario where hypernebulae accrete at a constant rate throughout their lives, with volumetric rates uniformly distributed across a range of mass-transfer rates $10^3 \lesssim \dot{m} \lesssim 10^7$, then their total contribution hypernebulae to the 10 TeV–1 PeV

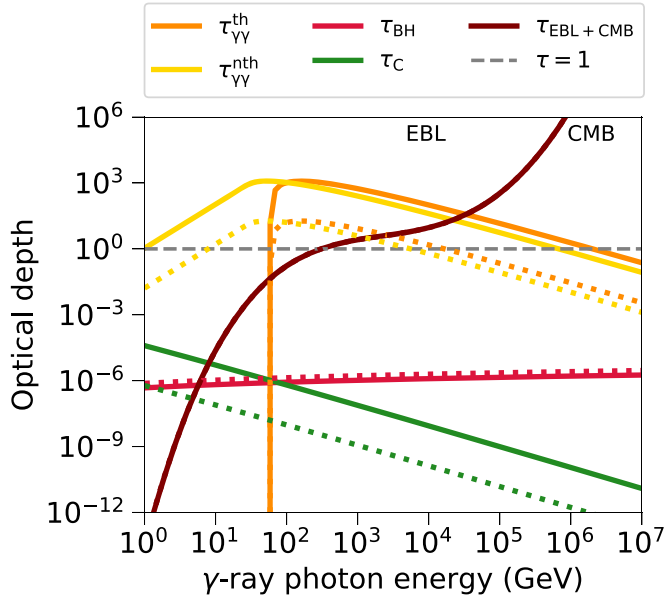

Figure 9. Optical depths of various interactions to gamma-ray photons with different energies. Solid and dotted curves are at times $t = t_{\rm active}$ (Equation (1)), and $t = t_{\rm free}$ (Equation (2)), respectively, for our fiducial model, but with the more relevant $\dot{m} = 10^7$ case. Orange and yellow curves represent $\gamma\gamma \rightarrow e^-e^+$ pair production with the accretion disk thermal (Equation (50)) and nonthermal Comptonized photons (Equation (51)), respectively; Bethe–Heitler interaction with the ions in the ejecta is represented by red curves (Equation (46)); green curves represent the Compton down-scattering in the Klein–Nishina regime with electrons in the ejecta (Equation (45)), and the interaction with extragalactic background light (EBL) and cosmic microwave background (CMB) radiation, for source at a redshift $z = 0.2$, is represented by maroon curves: the energies where EBL and CMB interactions dominate are noted near the top frame of the figure.

diffuse flux would be $\sim 25\%(\mathcal{R}_0/10^3\,{\rm Gpc^{-3}\,yr^{-1}})$, and will be dominated by the $\dot{m} \sim 10^7$ cases.

Throughout our analysis, we do not consider sources accreting at rates $\dot{m} \gg 10^7$ because their short lifetimes would preclude any proton from being accelerated to energies $\gtrsim 0.1E_{\rm thr}$ (Equation (23)) to engage in neutrino production through photomesonic channels (the factor of 0.1 accounts for $p\gamma$ interaction with the higher-energy nonthermal photons, which requires a smaller $E_{\rm thr}$; vertical gray region in Figure 8). In the following section, we consider the gamma-ray properties of the more relevant $\dot{m} = 10^7$ scenario.

4.3. γ-Ray Attenuation

The inevitable byproducts of neutrino production are gamma rays (from neutral pion decay; see Equation (36)(a)), with flux and spectral properties similar to those of neutrinos. The Fermi IGRB observations indicate a lower gamma-ray flux than that of neutrinos (Ackermann et al. 2015) suggesting that the primary sources of HE diffuse background neutrino should be faint gamma-ray emitters. In this section, we discuss the opacity of hypernebula to the gamma rays generated along with the neutrinos, and the impact of the intervening medium as the gamma rays propagate to Earth. The emitted gamma rays can be attenuated and reprocessed at least by the following three intrinsic processes, and Figure 9 shows some of the relevant optical depths at times $t = t_{\rm free}$, and $t = t_{\rm active}$.

(1) *Compton down-scattering*. The gamma-ray photons can lose energy and be attenuated by scattering off the electrons in the ejecta. The effective optical depth for the photons to lose most of their initial energy is (Vurm & Metzger 2021)

$$\tau_{\rm C} \simeq \frac{\dot{x}_{\rm C}}{c}\frac{R}{c}(1+\tau_{\rm KN}) \approx \tau_{\rm T}\frac{\ln(1+x)}{(1+3x)}\left[1+\frac{3\tau_{\rm T}}{8x}\ln\left(1+\frac{8x}{3}\right)\right]$$
$$\approx 10^{-9}\ln\left(\frac{x}{10^6}\right)\left(\frac{x}{10^6}\right)^{-1} \times \begin{cases} \dot{m}_5 v_{\rm w,9}^{-2}\left(\frac{t}{80\ {\rm yr}}\right)^{-2} & (t < t_{\rm free}) \\ \dot{m}_5^{1/5} v_{\rm w,9}^{2/5} n_1^{4/5}\left(\frac{t}{80\ {\rm yr}}\right)^{3/5} & (t > t_{\rm free}), \end{cases} \quad (45)$$

where $\tau_{\rm KN}$ is the Klein–Nishina optical depth for gamma-ray photons with dimensionless energies $x \equiv E_\gamma/m_{\rm e}c^2 \gg 1$ (Klein & Nishina 1929); the factor $1+\tau_{\rm KN}$ accounts for the diffusion time of the photons through the ejecta. $\tau_{\rm T} \sim n_{\rm e}\sigma_{\rm T}R$ is the Thomson optical depth with a scattering cross section $\sigma_{\rm T} = 6.6\times10^{-25}\,{\rm cm^{-2}}$ for an electron number density $n_{\rm e} \sim n_{\rm p}$, and the particle energy loss rate is $\dot{x}_{\rm C}/x \approx c\sigma_{\rm T}n_{\rm e}\ln(1+x)/(1+3x)$. Clearly, even the low-energy ($E_\gamma \sim 1$ GeV) gamma-ray photons do not suffer any losses due to Compton scattering, and the higher-energy photons only experience even lesser attenuation due to this process.

(2) *Bethe–Heitler process.* Gamma rays can be attenuated due to pair production upon interaction with relativistic ions in the ejecta (Bethe & Heitler 1934). The corresponding optical depth is given by Chodorowski et al. (1992),

$$\tau_{\rm BH} = n_{\rm p}\sigma_{\rm BH}R \approx 10^{-5}\ln\left(\frac{x}{10^6}\right) \times \begin{cases} \dot{m}_5 v_{\rm w,9}^{-2}\left(\frac{t}{80\ {\rm yr}}\right)^{-2} & (t<t_{\rm free}) \\ \dot{m}_5^{1/5} v_{\rm w,9}^{2/5} n_1^{4/5}\left(\frac{t}{80\ {\rm yr}}\right)^{3/5} & (t>t_{\rm free}) \end{cases}. \quad (46)$$

The scattering cross section can be approximated as (Zdziarski & Svensson 1989)

$$\sigma_{\rm BH} \simeq \frac{3}{8\pi}\alpha\sigma_{\rm T}Z^2\left[\frac{28}{9}\ln(2x) - \frac{218}{27}\right]; \quad (47)$$

where $\alpha = 1/137$ is the fine structure constant, and Z is the atomic charge of the nuclei (we assume $Z \simeq 1$ for hydrogen-dominated composition).[10] We can see from Figure 9 that $\tau_{\rm BH}$ barely depends upon E_γ, and the effect of Bethe–Heitler process is negligible in attenuating the emitted gamma rays.

(3) $\gamma\gamma \rightarrow e^+e^-$ *pair production*. Gamma rays pair produce upon interacting with ambient low-energy photons (Breit & Wheeler 1934). Assuming, for simplicity, a monochromatic isotropic thermal ambient UV/X-ray photon field with an energy given by Equation (18), the energy of the gamma-ray photon E_γ at which the pair production cross-sectional $\sigma_{\gamma\gamma}$

[10] However, note that, if the donor star has lost a significant fraction of its envelope, then the nebula material might possess a heavier-than-solar composition. Nonetheless, this will not qualitatively change our conclusion that Bethe–Heitler absorption is negligible.

peaks is

$$E_{\gamma,\rm pk} = \frac{4m_e^2c^4}{k_B T_{\rm eff}} \approx 60\ {\rm GeV}(1+\ln\dot{m}_7)^{1/4}\dot{m}_7^{1/4}\left(\frac{v_j}{0.3c}\right)^{-1/2}. \quad (48)$$

The scattering cross section can be taken as a smoothly connected piece-wise function such that (Svensson 1987)

$$\sigma_{\gamma\gamma} \sim \frac{3\sigma_T}{16} \times \begin{cases} 0 (E_\gamma < E_{\gamma,\rm pk}/4) \\ 1 (E_\gamma = E_{\gamma,\rm pk}) \\ \ln(x)/x (E_\gamma > E_{\gamma,\rm pk}) \end{cases}. \quad (49)$$

With this, the optical depth to $\gamma\gamma$ pair production with thermal photons can be estimated as

$$\tau_{\gamma\gamma}^{\rm th} = n_X^{\rm th}\sigma_{\gamma\gamma}R \approx 13\ln\left(\frac{x}{10^6}\right)\left(\frac{x}{10^6}\right)^{-1}(1+\ln\dot{m}_7)^{5/4}\dot{m}_7^{5/4} \times\left(\frac{v_j}{0.3c}\right)^{-1/2} \times \begin{cases} v_{w,9}^{-1}\left(\frac{t}{80\ {\rm yr}}\right)^{-1} & (t<t_{\rm free}) \\ \dot{m}_7^{-1/5}v_{w,9}^{-2/5}n_1^{1/5}\left(\frac{t}{80\ {\rm yr}}\right)^{3/5} & (t>t_{\rm free}) \end{cases}. \quad (50)$$

Likewise, one can also define an optical depth for $\gamma\gamma$ pair production with nonthermal photons (see Section 2.2(2)),

$$\tau_{\gamma\gamma}^{\rm nth} = n_X^{\rm th}\left(\frac{\epsilon}{\epsilon_{\rm pk,th}^{\rm eff}}\right)^{-2}\sigma_{\gamma\gamma}[\epsilon]R, \quad (51)$$

where $\sigma_{\gamma\gamma}[\epsilon]$ is constructed by taking $E_{\gamma,pk} = 4m_e^2c^4/\epsilon$ for individual photons with energy ϵ in the nonthermal power-law distribution. Figure 9 shows that gamma-ray photons with energies in the range 1 GeV–1 PeV will be strongly attenuated within the hypernebula by $\gamma\gamma$ pair production: specifically, with interactions dominated by nonthermal photons in the energy range 1–60 GeV, and by thermal photons in the energy range 60 GeV–1 PeV. The intrinsic attenuation of > PeV gamma rays is in principle possible by their interaction with the radio synchrotron photons. However, their small number density $n_{\rm GHz} \lesssim 10^{-4}\ {\rm cm}^{-3}$ (Sridhar & Metzger 2022) would imply a $\gamma\gamma$ pair production optical depth of $\tau_{\gamma\gamma}^{\rm GHz} \ll 1$, and the higher-energy gamma rays ($E_\gamma \gtrsim 1$ PeV) would still escape freely. For our fiducial choice of parameters, as $\tau_C \ll 1$ (see Figure 9), no gamma-ray cascades would be generated in hypernebulae.

The escaping >PeV gamma-ray photons will interact with the extragalactic background light (EBL) and the cosmic microwave background (CMB) radiation on their way to Earth. The EBL is composed of the UV-optical-IR photons (0.1–1000 μm) emitted by stars and galaxies since the epoch of reionization, which can pair produce upon interaction with gamma rays with $E_\gamma \gtrsim 10$ TeV (Nikishov 1961; Gould & Schréder 1967a, 1967b, see also Equation (48)). In Figure 9, we show the optical depth of EBL and CMB photons (Stecker et al. 2006) to gamma rays, and show that all the escaping gamma rays from a hypernebula—which happen to have energies $E_\gamma >$ PeV—will be attenuated. At different locations, the nonlinear dynamics of the pair production involving processes such as inverse-Compton scattering ($e\gamma \to e\gamma$) and triple pair production process ($e\gamma \to ee^+e^-$) can initiate electromagnetic cascades until the energy of the later generation of particles falls below the threshold to sustain these reactions. As a result, the injected PeV gamma rays could eventually appear at 10–100 GeV, with a spectral shape independent of the injected gamma-ray injection spectrum and the target soft photon spectrum (Berezinskii & Smirnov 1975) and a flux below the Fermi IGRB (Fang et al. 2022).

5. Conclusions

We have developed a model for HE neutrino emission from *hypernebulae*. A hypernebula is a new class of spatially compact ($\lesssim$pc), decades–millenia long transient "bubble" inflated by hyper-Eddington accredion disk winds that are more powerful than the typical ultra luminous X-ray sources (Sridhar & Metzger 2022). The rapid runaway mass transfer ($\dot{m} \sim 10^3$–10^7) onto a stellar mass compact object (black hole or a neutron star) required to inflate hypernebulae is naturally expected from an evolved companion star (e.g., imminent giant) leading up to a common-envelope event. For the purpose of our *proof-of-concept* calculations, we consider a fiducial binary containing a massive star ($M_\star = 30\ M_\odot$) accreting onto a black hole of fixed mass ($M_\bullet = 10\ M_\odot$), whose active duration is varied by varying the accretion rate ($10^3 < \dot{m} < 10^7$). The intrinsic properties of the hypernebula, and the observables of the neutrino emission (light curves, energy spectra, volume-integrated observed flux) are continuously evaluated across the free-expansion, deceleration, and post-active phases, as a function of the slow, wide-angled disk wind ($\dot{M} \sim \dot{M}_w$, v_w), and the fast, collimated disk wind and/or jet ($\eta = \dot{M}_j/\dot{M}$, v_j, σ_j) properties. The take-away results of this paper are as follows:

(1) The primary source of neutrino production in this model is the adiabatic fast wind/jet termination shock, where the shock-accelerated protons produce pions (that eventually decay into neutrinos) upon their photohadronic ($p\gamma$) interactions with the thermal and nonthermal X-ray photons from the accretion disk. The hadronic (pp) interactions play a subdominant role except during the late stages of a hypernebula's lifetime, particularly for low $\dot{m}$ systems.

(2) The highest-energy neutrinos are emitted during the end of a hypernebula's lifetime (when they are the largest in size). The maximum energy is found to be ~300 PeV for $\dot{m} = 10^5$ case. UHE neutrinos are highly sought-after over the past half of a century, and are likely to be discovered within the next couple of decades by upcoming neutrino observatories (Branco Valera et al. 2022) such as CHANT (Neronov et al. 2017), Trinity (Nepomuk Otte et al. 2019), GRAND (Álvarez-Muñiz et al. 2020), IceCube-Gen2 (IceCube-Gen2 Collaboration et al. 2014; Aartsen et al. 2021), Askaryan Radio Array (ARA Collaboration et al. 2012), and the ARIANNA detectors (Barwick et al. 2015). Hypernebulae are promising candidates for diffuse extragalactic ($\ll$EeV) UHE neutrinos.

(3) A distinct feature of hypernebulae as neutrino sources is their property of robust minimum neutrino energy, which is set solely by the steady background photon energies: the thermal photons set the prominent ~100 TeV low-energy spectral turnover, the nonthermal photons introduce a turnover at ~10 TeV, and the pp interactions set the lowest-energy turnover at 135 MeV. IceCube-DeepCore (Abbasi et al. 2012), KM3NeT (Adrián-Martínez et al. 2016; Fermani 2020, being built in the Mediterranean Sea), and the Gigaton Volume Detector (in Lake Baikal; Allakhverdyan et al. 2021) may

extend and improve the current neutrino sensitivities to sub-TeV regime. These facilities will be able to test the hypernebula model by better characterizing the TeV and sub-TeV spectrum of the HE diffuse background neutrinos.

(4) Assuming that the volumetric rates of hypernebulae follow common envelope events involving compact objects, an engine accreting at $\dot{m} = 10^7$ could comfortably explain $\sim$100% of the HE diffuse background neutrino flux. In a more realistic scenario, if the volumetric rate of hypernebulae were to be uniformly distributed among different accretion rate engines $10^3 < \dot{m} < 10^7$, hypernebulae could explain (depending on the mass-transfer rate) $\sim 25\%(\mathcal{R}_0/10^3\ \mathrm{Gpc^{-3}\ yr^{-1}})$ of the observed neutrino flux.

(5) The gamma rays that are inevitably produced along with neutrinos are attenuated within the hypernebulae primarily by the Breit–Wheeler $\gamma\gamma \rightarrow e^+e^-$ annihilation process. The gamma-ray photons in the energy range $1 < E_\gamma/\mathrm{GeV} < 60$ are attenuated by nonthermal background photons, and the higher-energy gamma rays $60 < E_\gamma/\mathrm{GeV} < 10^6$ are attenuated by thermal background photons. The escaping >PeV gamma rays will be attenuated by their interaction with the EBL. Therefore, hypernebulae are gamma-ray faint sources of neutrino emission, thus satisfying the IGRB constraints of Fermi/LAT.

Finally, we would like to emphasize that hypernebulae are radio-synchrotron-bright objects that can be detected as point sources with all-sky radio surveys such as FIRST (Becker et al. 1995) or VLASS (Lacy et al. 2020). A detailed study of the electromagnetic counterparts to hypernebulae—including light curves, spectra—can be found in Sridhar & Metzger (2022). A population of FRBs could be powered by flares along hyper-Eddington accretion disk jets (Sridhar et al. 2021a; Bhandari et al. 2023). Recently, Abbasi et al. (2023a) presented the search results for spatially and temporally coincident neutrino emission from FRBs with IceCube Cascade data, and found no significant clustering around the short-lived and beamed FRB event. This result is in agreement with theoretical predictions (Metzger et al. 2020). However, in a scenario of accretion-powered FRBs, the hypernebula surrounding the central FRB engine could serve as a persistent radio, and neutrino source, thus also contributing to the HE diffuse background neutrino flux.

Acknowledgments

N.S. acknowledges the hospitality of the Department of Astronomy at Cornell University, and the Center for Cosmology and AstroParticle Physics at The Ohio State University for their generous hospitality, where parts of this work were conceived. N.S. would like to thank John Beacom, Damiano Fiorillo, and Todd Thompson for fruitful discussions, and thank Stephanie Wissel for sharing the details on various neutrino experiments' sensitivities. N.S. acknowledges the support from NASA (grant No. 80NSSC22K0332), NASA FINESST (grant No. 80NSSC22K1597), and Columbia University Dean's fellowship. B.D.M. acknowledges support from the National Science Foundation (AST-2009255). K.F. is supported by the Office of the Vice Chancellor for Research and Graduate Education at the University of Wisconsin-Madison with funding from the Wisconsin Alumni Research Foundation. K.F. acknowledges support from NASA (80NSSC22K1584) and National Science Foundation (PHY-2110821).

Appendix A
Timescales

A list of all the relevant timescales of the model introduced in this paper, and their definitions, is provided in Table 1.

Table 1
Model Timescales

Variable	C.f.	Definition
$t_{\rm cross}$	Figure 3	Light-crossing timescale of the hypernebula.
$t_{\rm active}$	Equation (1)	Active duration of the dynamically unstable accretion phase at a mass-transfer rate of $\dot{M}$.
$t_{\rm free}$	Equation (2)	Free-expansion timescale beyond which the wind ejecta shell starts decelerating.
$t_{\rm exp}$	Equation (5)	Expansion timescale of the shocked gas.
$t_{\rm cool}$	Equation (10)	Cooling timescale of the shock-heated gas.
$t_{\rm rad}^{\rm fs}$	Equation (12)	The time after which the forward shock becomes radiative.
$t_{\rm cross}^{\rm cone}$	Equation (25)	The time particles spend within the solid angle of background X-ray photon field.
$t_{\rm p\gamma}^{\rm (th,nth)}$	Equation (26)	Cooling time due to photomeson interaction between protons and background thermal and nonthermal photon fields.
$t_{\rm pp}$	Equation (27)	Hadronuclear interaction timescale.
$t_{\pi,\rm cre}$	Equation (28)	Pion creation timescale.
$t_{\rm p,syn}$	Equation (29)	Proton synchrotron cooling timescale.
$\tau_{\pi,\mu}$	Equation (31)	Decay times of pions and muons.
$t_{\rm acc}$	Equation (34)	Diffusive shock acceleration timescale.

Appendix B
Proton Energy Spectra

The temporal evolution of the JTS-energized proton energy spectra is shown in Figure 6, for different $\dot{m}$. The thermal population of protons occupies a distinct hump in the energy spectrum at $E \sim 3\bar{E} \sim 10^{-2}$ GeV (see Equation (9)). At $t \sim t_{\rm free}$ (dotted curves), both the spectral HE cutoff, $E_{\rm max}(t)$, and the spectral normalization increase with $\dot{m}$. However, at later times $t \sim t_{\rm active}$ (solid curves), the protons accelerated by the higher-$\dot{m}$ engines are less energetic than the lower-$\dot{m}$ cases given the shorter lifetimes of the former, and the resulting size-limited energization constraints (Hillas 1984). This reduces the HE spectral cutoff for high-$\dot{m}$ cases while retaining a constant $E_{\rm thr}$. This limits neutrino production only to cases with $\dot{m} \lesssim$ few $\times\ 10^7$ (see also Figure 8).

Appendix C
Hypernebula Parameter Exploration

Figure 10 shows the influence of each relevant physical parameter of hypernebula on the model neutrino flux, for $\dot{m} = 10^7$. As mentioned in Section 4.2, Figure 10 demonstrates the robustness of the low-energy turnovers for a wide range of hypernebula parameter space. The neutrino flux due to hadronuclear interactions (few $\times\ 10^{-10}\,\mathrm{GeV\,s^{-1}\,cm^{-2}\,sr^{-1}}$ at $\lesssim 10^2$ GeV) is not strongly affected by any parameter except for η, which proportionately scales the normalization of the model flux at all energies as it changes only the JTS power (panel (f)). As a result, the cases with $\eta \sim 1$ might overproduce not only the PeV neutrino flux but also the diffuse gamma-ray flux. When $v_{\rm w} \ll v_{\rm j}$, an increase in $v_{\rm w}$ increases the shell radius and therefore the shock luminosity, but a further increase ($v_{\rm w} \lesssim v_{\rm j}$) would mean a slower JTS (i.e., $v_{\rm j} - v_{\rm fs}$), and a lower $n_{\rm p}$

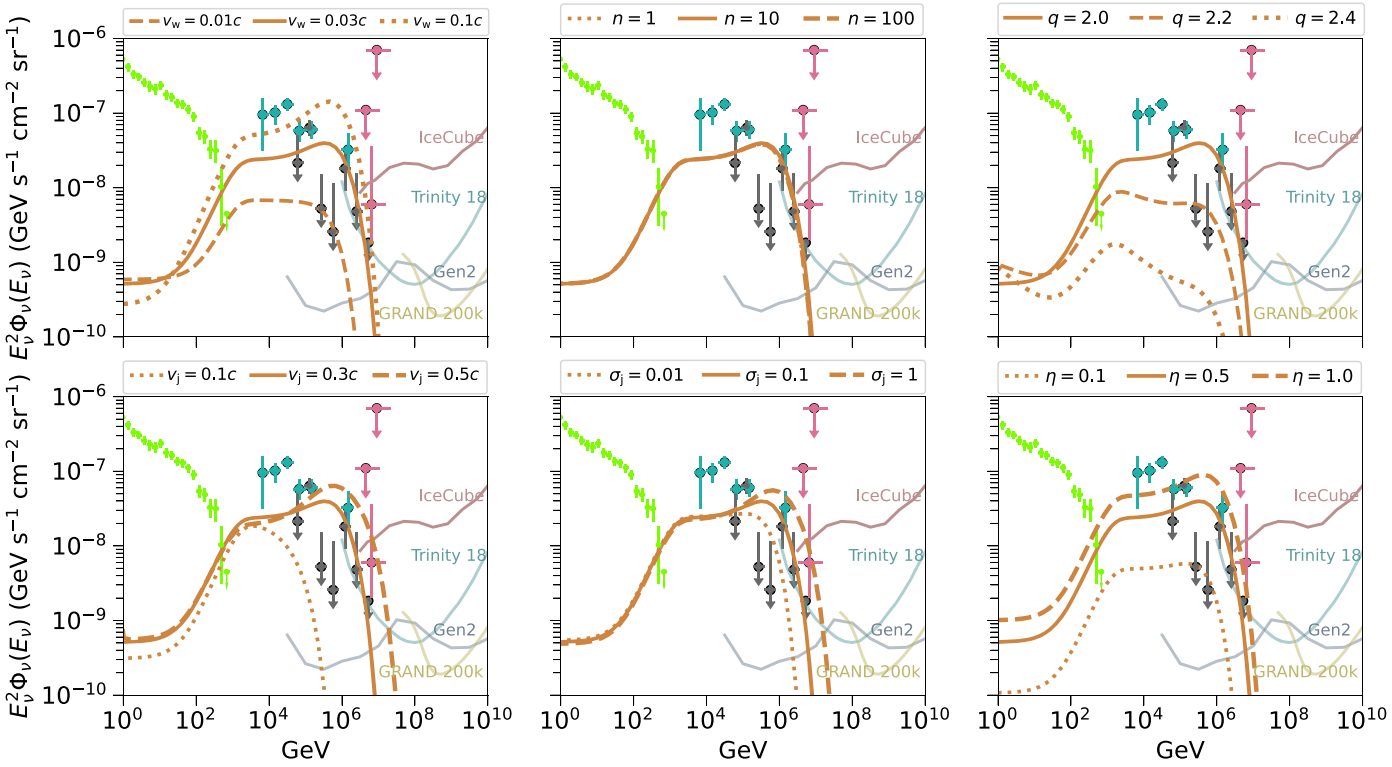

Figure 10. Neutrino flux models for a range of hypernebula's physical parameters. The fiducial model is represented by solid brown curve in all the panels (but with $\dot{m} = 10^7$; see also Section 2). The dashed and dotted curves in each panel show how altering one parameter (that is mentioned above each panel) changes the observed flux about the fiducial model. See Figure 7 for a description of the other labels and markers in each panel.

(Equation (7)), which will sharply decrease the (photohadronic contribution to the) neutrino flux, and $E_{\rm max}$ (panel (a)). An increase in $v_{\rm j}$, on the other hand, monotonically increases $E_{\rm max}$, and the overall flux normalization—primarily by boosting the neutrino production through thermal photohadronic interactions (panel (d)). On the other hand, $\sigma_{\rm j}$ solely affects the HE cutoff (panels (b) and (e)). An increase in the proton spectral index q steepens the neutrino spectrum by decreasing the thermal photohadronic component (hump at $\sim$1 PeV) more than the nonthermal photohadronic component (hump at $\sim$1 TeV) of the neutrino spectrum (panel (c)). While in principle, an increase in the upstream density increases the neutrino flux and HE cutoff, it has the least influence on the overall flux ($B_{\rm jts} \propto n^{1/5}$; see Equation (13)). The parameter exploration in Figure 10 suggests that hypernebulae—with $v_{\rm w}/c > 0.1$, $v_{\rm j}/c \sim 0.5$, $n \gtrsim 100\,{\rm cm}^{-3}$, and $\sigma_{\rm j} \gtrsim 1$—could be promising candidates for $\gtrsim$100 PeV UHE neutrinos that could be detected by future facilities such as IceCube-Gen2 (IceCube-Gen2 Collaboration et al. 2014; Aartsen et al. 2021), Trinity (Nepomuk Otte et al. 2019), perhaps GRAND (Álvarez-Muñiz et al. 2020).

ORCID iDs

Navin Sridhar https://orcid.org/0000-0002-5519-9550
Brian D. Metzger https://orcid.org/0000-0002-4670-7509
Ke Fang https://orcid.org/0000-0002-5387-8138

References

Aartsen, M. G., Abbasi, R., Abdou, Y., et al. 2013, PhRvL, 111, 021103
Aartsen, M. G., Abbasi, R., Ackermann, M., et al. 2021, JPhG, 48, 060501
Aartsen, M. G., Abraham, K., Ackermann, M., et al. 2016, ApJ, 824, 115
Aartsen, M. G., Ackermann, M., Adams, J., et al. 2017, ApJ, 849, 67
Aartsen, M. G., Ackermann, M., Adams, J., et al. 2020, PhRvL, 124, 051103
Abbasi, R., Abdou, Y., Abu-Zayyad, T., et al. 2012, APh, 35, 615
Abbasi, R., Ackermann, M., Adams, J., et al. 2021, PhRvD, 104, 022002
Abbasi, R., Ackermann, M., Adams, J., et al. 2021a, PhRvD, 104, 022002
Abbasi, R., Ackermann, M., Adams, J., et al. 2021b, PhRvD, 104, 022002
Abbasi, R., Ackermann, M., Adams, J., et al. 2022, ApJ, 928, 50
Abbasi, R., Ackermann, M., Adams, J., et al. 2023a, ApJ, 946, 80
Abbasi, R., Ackermann, M., Adams, J., et al. 2023b, ApJL, 949, L12
Abolmasov, P., Fabrika, S., Sholukhova, O., & Kotani, T. 2008, arXiv:0809.0409
Ackermann, M., Ajello, M., Albert, A., et al. 2015, ApJ, 799, 86
Adrián-Martínez, S., Ageron, M., Aharonian, F., et al. 2016, JPhG, 43, 084001
Albert, A., André, M., Anghinolfi, M., et al. 2018, ApJL, 868, L20
Albert, A., André, M., Anghinolfi, M., et al. 2021, MNRAS, 500, 5614
Allakhverdyan, V. A., Avrorin, A. D., Avrorin, A. V., et al. 2021, PAN, 84, 1600
Álvarez-Muñiz, J., Alves Batista, R., Balagopal, V. A, et al. 2020, SCPMA, 63, 219501
ARA Collaboration, Allison, P., Auffenberg, J., et al. 2012, APh, 35, 457
Baikal Collaboration, Allakhverdyan, V. A., Avrorin, V. D., et al. 2023, PhRvD, 107, 042005
Barwick, S. W., Berg, E. C., Besson, D. Z., et al. 2015, APh, 70, 12
Becker, J. K. 2008, PhR, 458, 173
Becker, R. H., White, R. L., & Helfand, D. J. 1995, ApJ, 450, 559
Begelman, M. C., King, A. R., & Pringle, J. E. 2006, MNRAS, 370, 399
Berezinskii, V. S., Bulanov, S. V., Dogiel, V. A., & Ptuskin, V. S. 1990, Astrophysics of Cosmic Rays (Amsterdam: North-Holland)
Berezinskii, V. S., & Smirnov, A. I. 1975, Ap&SS, 32, 461
Bethe, H., & Heitler, W. 1934, RSPSA, 146, 83
Bhandari, S., Gordon, A. C., Scott, D. R., et al. 2023, ApJ, 948, 67
Bhattacharya, M., Alonso Carpio, J., Murase, K., & Horiuchi, S. 2023, MNRAS, 521, 2391
Blandford, R., & Eichler, D. 1987, PhR, 154, 1
Blandford, R. D., & Begelman, M. C. 1999, MNRAS, 303, L1
Blandford, R. D., & Ostriker, J. P. 1978, ApJL, 221, L29
Branco Valera, V., Bustamante, M., & Glaser, C. 2022, arXiv:2210.03756
Breit, G., & Wheeler, J. A. 1934, PhRv, 46, 1087
Briel, M. M., Eldridge, J. J., Stanway, E. R., Stevance, H. F., & Chrimes, A. A. 2022, MNRAS, 514, 1315

Capanema, A., Esmaili, A., & Murase, K. 2020, PhRvD, 101, 103012
Capanema, A., Esmaili, A., & Serpico, P. D. 2021, JCAP, 2021, 037
Caprioli, D., & Spitkovsky, A. 2014, ApJ, 794, 47
Chakraborti, S., Ray, A., Soderberg, A. M., Loeb, A., & Chandra, P. 2011, NatCo, 2, 175
Chang, P.-W., Zhou, B., Murase, K., & Kamionkowski, M. 2022, arXiv:2210.03088
Chatterjee, S., Law, C. J., Wharton, R. S., et al. 2017, Natur, 541, 58
Chodorowski, M. J., Zdziarski, A. A., & Sikora, M. 1992, ApJ, 400, 181
Comisso, L., & Sironi, L. 2022, ApJL, 936, L27
Coppejans, D. L., Margutti, R., Terreran, G., et al. 2020, ApJL, 895, L23
Dai, L., & Fang, K. 2017, MNRAS, 469, 1354
Dermer, C. D., & Atoyan, A. 2003, PhRvL, 91, 071102
Diesing, R., & Caprioli, D. 2021, ApJ, 922, 1
Draine, B. T. 2011, Physics of the Interstellar and Intergalactic Medium (Princeton, NJ: Princeton Univ. Press)
Eichler, D. 1979, ApJ, 232, 106
Eichmann, B., Oikonomou, F., Salvatore, S., Dettmar, R. J., & Tjus, J. B. 2022, ApJ, 939, 43
Eidelman, S., Hayes, K. G., Olive, K. A., et al. 2004, PhLB, 592, 1
Fang, K., Gallagher, J. S., & Halzen, F. 2022, ApJ, 933, 190
Fang, K., & Metzger, B. D. 2017, ApJ, 849, 153
Fang, K., Metzger, B. D., Vurm, I., Aydi, E., & Chomiuk, L. 2020, ApJ, 904, 4
Fang, K., & Murase, K. 2021, ApJ, 919, 93
Fasano, M., Celli, S., Guetta, D., et al. 2021, JCAP, 2021, 044
Fermani, P. 2020, in Proc. 21st Int. Workshop on Neutrinos from Accelerators —PoS (NuFact2019), 369, ed. M. Lee & U. Yang (Trieste: SISSA), 32
Gould, R. J., & Schréder, G. P. 1967a, PhRv, 155, 1404
Gould, R. J., & Schréder, G. P. 1967b, PhRv, 155, 1408
Grichener, A., & Soker, N. 2021, MNRAS, 507, 1651
Guetta, D., & Granot, J. 2003, ApJ, 585, 885
Guo, G., Qian, Y. -z., & Wu, M. R. 2023, PhRvD, 108, L021303
Hashizume, K., Ohsuga, K., Kawashima, T., & Tanaka, M. 2015, PASJ, 67, 58
Hillas, A. M. 1984, ARA&A, 22, 425
Ho, A. Y. Q., Perley, D. A., Gal-Yam, A., et al. 2023, ApJ, 949, 120
Ho, A. Y. Q., Perley, D. A., Kulkarni, S. R., et al. 2020, ApJ, 895, 49
IceCube Collaboration, Aartsen, M. G., Abbasi, R., et al. 2021, Natur, 591, 220
IceCube Collaboration, Aartsen, M. G., Ackermann, M., et al. 2001, arXiv:2001.09520
IceCube Collaboration, Aartsen, M. G., Ackermann, M., et al. 2018a, arXiv:1808.07629
IceCube Collaboration, Aartsen, M. G., Ackermann, M. G., et al. 2018b, Sci, 361, 147
IceCube Collaboration, Aartsen, M. G., Ackermann, M., et al. 2018c, Sci, 361, eaat1378
IceCube Collaboration, Abbasi, R., Ackermann, M., et al. 2022, Sci, 378, 538
IceCube-Gen2 Collaboration, Aartsen, M. G, Ackermann, M., et al. 2014, arXiv:1412.5106
Inoue, S., Cerruti, M., Murase, K., & Liu, R. Y. 2022, arXiv:2207.02097
Inoue, Y., Lee, S. H., Tanaka, Y. T., & Kobayashi, S. B. 2017, APh, 90, 14
Jacobsen, I. B., Wu, K., On, A. Y. L., & Saxton, C. J. 2015, MNRAS, 451, 3649
Jaroschewski, I., Becker Tjus, J., & Biermann, P. L. 2023, MNRAS, 518, 6158
Kahabka, P. 2006, AdSpR, 38, 2836
Karambelkar, V. R., Kasliwal, M. M., Blagorodnova, N., et al. 2023, ApJ, 948, 137
Kelner, S. R., & Aharonian, F. A. 2008, PhRvD, 78, 034013
Kimura, S. S. 2022, arXiv:2202.06480
King, A. R. 2009, MNRAS, 393, L41
Klein, O., & Nishina, T. 1929, ZPhy, 52, 853
Kobayashi, H., Ohsuga, K., Takahashi, H. R., et al. 2018, PASJ, 70, 22
Kun, E., Bartos, I., Becker Tjus, J., et al. 2022, ApJ, 934, 180
Lacy, M., Baum, S. A., Chandler, C. J., et al. 2020, PASP, 132, 035001
Liodakis, I., Hovatta, T., Pavlidou, V., et al. 2022, A&A, 666, A36
Loeb, A., & Waxman, E. 2006, JCAP, 2006, 003
Lunardini, C., & Winter, W. 2017, PhRvD, 95, 123001
Mannheim, K., & Biermann, P. L. 1989, A&A, 221, 211
Mészáros, P., & Waxman, E. 2001, PhRvL, 87, 171102
Metzger, B. D. 2022, ApJ, 932, 84
Metzger, B. D., Fang, K., & Margalit, B. 2020, ApJL, 902, L22
Mićić, M., Irwin, J. A., & Lin, D. 2022, ApJ, 928, 117
Murase, K. 2017, in Neutrino Astronomy: Current Status, Future Prospects, ed. T. Gaisser & A. Karle (Singapore: World Scientific), 15
Murase, K. 2018, PhRvD, 97, 081301
Murase, K., Guetta, D., & Ahlers, M. 2016, PhRvL, 116, 071101
Murase, K., Kimura, S. S., & Mészáros, P. 2020, PhRvL, 125, 011101
Murase, K., Thompson, T. A., Lacki, B. C., & Beacom, J. F. 2011, PhRvD, 84, 043003
Nepomuk Otte, A., Brown, A. M., Falcone, A. D., Mariotti, M., & Taboada, I. 2019, arXiv:1907.08732
Neronov, A., Semikoz, D. V., Anchordoqui, L. A., Adams, J. H., & Olinto, A. V. 2017, PhRvD, 95, 023004
Nikishov, A. 1961, Zhur. Eksptl'. i Teoret. Fiz., 41, 549
Niu, C. H., Aggarwal, K., Li, D., et al. 2022, Natur, 606, 873
Paczynski, B., & Xu, G. 1994, ApJ, 427, 708
Pakull, M. W., Soria, R., & Motch, C. 2010, Natur, 466, 209
Pavlovskii, K., Ivanova, N., Belczynski, K., & Van, K. X. 2017, MNRAS, 465, 2092
Perley, D. A., Mazzali, P. A., Yan, L., et al. 2019, MNRAS, 484, 1031
Pinto, C., & Kosec, P. 2023, AN, 344, e20220134
Poutanen, J., Lipunova, G., Fabrika, S., Butkevich, A. G., & Abolmasov, P. 2007, MNRAS, 377, 1187
Prentice, S. J., Maguire, K., Smartt, S. J., et al. 2018, ApJL, 865, L3
Planck Collaboration, Aghanim, N., Akrami, N., et al. 2020, A&A, 641, A6
Razzaque, S., Mészáros, P., & Waxman, E. 2004, PhRvL, 93, 181101
Ripperda, B., Bacchini, F., & Philippov, A. A. 2020, ApJ, 900, 100
Roepke, F. K., & De Marco, O. 2023, LRCA, 9, 2
Romero, G. E., & Torres, D. F. 2003, ApJL, 586, L33
Sadowski, A., & Narayan, R. 2015, MNRAS, 453, 3213
Safi-Harb, S., Mac Intyre, B., Zhang, S., et al. 2022, ApJ, 935, 163
Sarmah, P., Chakraborty, S., Tamborra, I., & Auchettl, K. 2022, JCAP, 2022, 011
Schrøder, S. L., MacLeod, M., Loeb, A., Vigna-Gómez, A., & Mandel, I. 2020, ApJ, 892, 13
Schure, K. M., Kosenko, D., Kaastra, J. S., Keppens, R., & Vink, J. 2009, A&A, 508, 751
Secunda, A., Bellovary, J., Mac Low, M. M., et al. 2020, ApJ, 903, 133
Selina, R. J., Murphy, E. J., McKinnon, M., et al. 2018, Proc. SPIE, 10700, 107001O
Senno, N., Mészáros, P., Murase, K., Baerwald, P., & Rees, M. J. 2015, ApJ, 806, 24
Senno, N., Murase, K., & Mészáros, P. 2017, ApJ, 838, 3
Sironi, L., & Beloborodov, A. M. 2020, ApJ, 899, 52
Sironi, L., & Spitkovsky, A. 2011, ApJ, 726, 75
Soker, N. 2022, RAA, 22, 122003
Sridhar, N., & Metzger, B. D. 2022, ApJ, 937, 5
Sridhar, N., Metzger, B. D., Beniamini, P., et al. 2021a, ApJ, 917, 13
Sridhar, N., Sironi, L., & Beloborodov, A. M. 2021b, MNRAS, 507, 5625
Sridhar, N., Sironi, L., & Beloborodov, A. M. 2023, MNRAS, 518, 1301
Stecker, F. W. 1968, PhRvL, 21, 1016
Stecker, F. W., Done, C., Salamon, M. H., & Sommers, P. 1991, PhRvL, 66, 2697
Stecker, F. W., Malkan, M. A., & Scully, S. T. 2006, ApJ, 648, 774
Strolger, L. G., Dahlen, T., Rodney, S. A., et al. 2015, ApJ, 813, 93
Strolger, L. G., Riess, A. G., Dahlen, T., et al. 2004, ApJ, 613, 200
Svensson, R. 1987, MNRAS, 227, 403
Thompson, T. A., Quataert, E., Waxman, E., & Loeb, A. 2006, arXiv:astro-ph/0608699
Toalá, J. A., & Arthur, S. J. 2011, ApJ, 737, 100
Urquhart, R., Soria, R., Johnston, H. M., et al. 2018, MNRAS, 475, 3561
Vigna-Gómez, A., Neijssel, C. J., Stevenson, S., et al. 2018, MNRAS, 481, 4009
Vlasov, A., Vurm, I., & Metzger, B. D. 2016, MNRAS, 463, 394
Vurm, I., & Metzger, B. D. 2021, ApJ, 917, 77
Wang, X. Y., & Liu, R. Y. 2016, PhRvD, 93, 083005
Waxman, E., & Bahcall, J. 1997, PhRvL, 78, 2292
Waxman, E., & Bahcall, J. 1998, PhRvD, 59, 023002
Weaver, R., McCray, R., Castor, J., Shapiro, P., & Moore, R. 1977, ApJ, 218, 377
Zdziarski, A. A., & Svensson, R. 1989, ApJ, 344, 551